Effect of microstructure induced anisotropy on fatigue behaviour of functionally graded Inconel 718 fabricated by additive manufacturing

Ghorbanpour, Saeede; Sahu, Saswat; Deshmukh, Kaustubh; Borisov, Evgenii; Riemslag, Ton; Reinton, Elise; Bertolo, Virginia; Jiang, Quanxin; Popovich, Anatolii; Shamshurin, Aleksey

DOI
10.1016/j.matchar.2021.111350

Publication date
2021

Document Version
Final published version

Published in
Materials Characterization

Materials Characterization 179 (2021) 111350

Contents lists available at ScienceDirect

Materials Characterization

journal homepage: www.elsevier.com/locate/matchar

Effect of microstructure induced anisotropy on fatigue behaviour of functionally graded Inconel 718 fabricated by additive manufacturing

Saeede Ghorbanpour [a,*], Saswat Sahu [a], Kaustubh Deshmukh [a], Evgenii Borisov [b], Ton Riemslag [a], Elise Reinton [a], Virginia Bertolo [a], Quanxin Jiang [a], Anatolii Popovich [b], Aleksey Shamshurin [b], Marko Knezevic [c], Vera Popovich [a,b,*]

[a] Department of Materials Science and Engineering, Delft University of Technology, the Netherlands
[b] Peter the Great Saint-Petersburg Polytechnic University, Saint Petersburg, Russia
[c] Department of Mechanical Engineering, University of New Hampshire, Durham, NH 03824, USA

ARTICLE INFO

Keywords:
Laser powder bed fusion
Inconel 718
Fatigue behaviour
Functionally graded materials
Microstructural anisotropy

ABSTRACT

In this paper, the effect of microstructural anisotropy on the fatigue crack growth behaviour of the functionally graded Inconel 718 fabricated through laser powder bed fusion (L-PBF) is investigated. Different manufacturing parameters, including low and high laser powers, were used to produce a variety of non-graded (NG) and functionally graded (G) specimens in two build directions, vertical and horizontal. In addition, a group of heat treated wrought samples was tested as a reference. It was observed that the different manufacturing parameters result in various grain size, crystallographic textures, precipitates and Laves phases, porosity, and un-melted particles. Three-point bending fatigue tests were conducted to measure the threshold stress intensity factor (ΔK_{th}) and fatigue crack growth rate (FCGR),da/dN. Only the lower laser power L-BPF Inconel material was found to have comparable to the wrought heat treated material fatigue crack growth behaviour. Furthermore, a new approach of automatically controlling ΔK as a function of the crack length was employed for graded specimens to investigate the crack growth rate as a function of local microstructure. The FCGR value of the vertical L-PBF samples, in which the crack direction was perpendicular to the build direction, remained constant. In contrast, the da/dN value of the horizontal samples with the crack direction parallel to the build direction increased constantly with the increase of the crack length. This behaviour is in good agreement with the hardness profile of the graded materials. Melt pool boundaries, graded interface boundaries, and grain orientations close to ⟨001⟩ were found to deflect the crack path. Additionally, it was found that L-PBF material is more affected (at a low stress ratio of $R = 0.1$) by the roughness-induced crack closure than the wrought counterparts. This study has successfully demonstrated the feasibility of using an additive manufacturing process to fabricate functionally graded materials featuring tailorable fatigue response of the local microstructures.

1. Introduction

Inconel 718 (IN718), due to its outstanding combination of superior strength, creep and wear resistance, corrosion and oxidation, even at cryogenic and elevated temperatures (up to 650 °C), is widely used in various applications in petrochemical, aeronautics, energy, and aerospace industries [1–5]. IN718 is a precipitation hardened Nickel-base superalloy with main strengthening precipitates γ' (Ni_3Al) with an $L1_2$

Abbreviations: AM, additive manufacturing; AP, as-processed; BD, build direction; BEC, backscattered electron composition; CAD, computer aided design; CB, Crack branching; CD, crack direction; CI, confidence index; CS, cross snake; δ_{total}, load line displacement; ΔK, stress intensity range; ΔK_{th}, threshold stress intensity factor; DCPD, direct current potential drop; DIC, digital image correlation; E, Young's modulus; EBSD, electron backscattered diffraction; EDM, electrical discharge machining; EDS, Energy Dispersive X-Ray Spectroscopy; FCGR, fatigue crack growth rate; FGM, functionally graded materials; G, graded; GB, grain boundary; H, horizontal; IN718, Inconel 718; IPF, Inverse Pole Figure; LAGB, low angle grain boundaries; LCF, low cycle fatigue; LD, loading direction; LED, linear energy density; L-PBF, laser powder bed fusion; m.r.d., multiples of a random distribution; NG, non-graded; NNS, near net shape; PMMA, polymer clamp system; R, stress ratio; SEM, scanning electron microscopy; V, vertical; VED, volume energy density; XRD, X-ray diffraction.

* Corresponding authors at: Faculty of Mechanical, Maritime, and Materials Engineering, Delft University of Technology, The Netherlands.
E-mail addresses: S.Ghorbanpour@tudelft.nl (S. Ghorbanpour), v.popovich@tudelft.nl (V. Popovich).

https://doi.org/10.1016/j.matchar.2021.111350
Received 24 May 2021; Received in revised form 14 July 2021; Accepted 20 July 2021
Available online 24 July 2021

lattice structure and γ" (Ni_3Nb) with a DO_{22} structure [1,6–8]. γ' precipitates are spherical shape with diameters ranging between 10 and 40 nm, while γ" precipitates are disk shaped with diameters of 20–30 nm and thickness of 5–6 nm [2,9–12]. The weight percentages of γ' and γ" can vary around 3–8% and 8–18%, respectively, based on the manufacturing methods and post processing history [13,14]. In addition to the strengthening precipitates, undesired phases such as hexagonal Laves (Ni,Fe,Cr)2(Nb,Mo,Ti) and MC carbides could be present in the alloy [7,15].

IN718 also exhibits high low cycle fatigue (LCF) strength and high temperature fatigue crack growth resistance [1,16]. Some research [1,17–22] was performed on the short and long crack initiation and growth behaviour of conventionally manufactured IN718. Short crack initiation and growth of a solution treated forged IN718 were studied at 600 °C [17]. Due to mismatch strains between the oxidized particles and the matrix, crack initiation sites with sub-surface primary carbides (Nb, Ti) C oxidation were developed. Short crack growth rates (before reaching a couple of hundred microns) were found to be constant across a wide range of crack lengths. However, they transitioned to rapid and accelerating growth while the crack length increased to several hundred microns [17]. Room temperature fatigue crack growth was found to be transgranular with different crack growth mechanisms such as pure shearing on slip planes or formation of microcracks and subsequent linking [18]. The high temperature fatigue crack growth rate (FCGR) was studied in [1,19–21] and it was found that the FCGR increases with temperature. However, the high temperature fatigue behaviour of IN718 is not the scope of the current study. In addition to the test temperature, the microstructure can play an important role in the fatigue crack growth behaviour. Coarsening the grain size from 22 μm to 91 μm was found to reduce the near threshold crack growth rates while increases the threshold stress intensity factor [22].

Additive manufacturing (AM) has been considered a replacement manufacturing technique for conventional methods due to the near net shape (NNS) production capability, which is desirable for complicated geometries. Altering the manufacturing parameters can influence the microstructure and grain size and thus affect the mechanical properties of the final products. Different scanning strategies, namely cross snake (CS) and cross snake 10 (CS10), in the selective electron beam melting method results in columnar and equiaxed grains with significantly different sizes [23]. The AM process has been previously used to tailor the microstructure and develop site-specific and user-defined functional properties [24]. As reported in [24–26] the microstructure is affected by various AM methods and different manufacturing parameters, resulting in cube or Goss textures. Laser powder bed fusion (L-PBF) which is a common AM method employs a laser beam to melt powders layer by layer and build the final geometry defined by a computer aided design (CAD) model [24,27,28].

Since the AM methods became more widely used, more research has been focusing on the mechanical properties including the fatigue behaviour. Long crack propagation of L-PBF IN718 was formulated in the threshold and Paris regions in [28]. It was found that L-PBF IN718 is less resistant to the long crack growth in the near threshold region due to the effect of the residual stress, finer microstructure, and low content of boron [28]. Similarly, a higher crack growth rate compared to the wrought material was reported in the L-PBF IN718 with columnar grains and an average grain size of 100 μm on the building direction cross section [29]. In situ fatigue testing at 25 °C and 650 °C revealed that the fatigue short crack growth rates are much higher in the build direction (BD) due to the small misorientation of adjacent grains and the lower strength compared with the other orientations [30].

Functionally graded materials (FGM)s refer to a class of advanced materials with different compositions or microstructures along with the geometry, which results in different properties [31–33]. The transition of the microstructure, composition, and morphology can be used to grade the materials and functional properties [31]. FGM parts can be made from one material, single-material FGM, or different materials known as multi-material FGM. While the former can be used to achieve superior and functional properties, the latter can also be a means of joining dissimilar metals. In our earlier works, it was successfully demonstrated that the microstructure of IN718 can be graded by manipulation of L-PBF process parameters. It was shown [24,34,35] that Vickers hardness, tensile strength, and creep of the functionally graded IN718 can be tailored to achieve location-specific properties. However, the fatigue crack growth behaviour of the functionally graded IN718 material has not been investigated yet. Furthermore, the experimental approach to investigate the fatigue crack growth behaviour in functionally graded materials, which could account for dissimilar microstructures and interface behaviour has not been reported to date.

The objective of the current research is to study the effect of the grain size, texture, and graded interface on the fatigue crack growth behaviour of a functionally graded L-PBF IN718. Graded samples with different build orientations were manufactured employing the L-PBF technique. Additionally, a set of non-graded samples with a variety of grain sizes, textures and build directions were manufactured and studied. In addition, heat treated wrought samples (based on AMS 5663 [36]) were tested and the corresponding data were used as a reference. Interactions of fatigue crack path with various microstructural features and graded interface are studied in detail. Furthermore, a novel fatigue crack growth setup and approach are developed to account for the graded interface behaviour.

2. Materials and methods

2.1. Materials

The IN718 samples were manufactured using the powder produced by the gas atomization of the hot melt with a chemical composition of (wt%) 51.45 Ni, 19.38 Cr, 18.49 Fe, 5.3 Nb, 3.4 Mo, 1.04 Ti, 0.72 Al, 0.1 Co, and 0.12 Mn. The particle diameters of the powder ranged between $d_{10} = 20$ μm and $d_{90} = 64$ μm. Samples for this study were manufactured using the L-PBF technique with an SLM 280^{HL} facility (SLM Solutions Group AG, Germany). Two different laser power values of 250 W and 950 W with a wavelength of 1070 nm were employed to build the fatigue specimens. To optimise the manufacturing parameters, the linear energy density (LED), E_l, which is the ratio of the laser power to the laser scanning speed was adjusted and is defined by Eq. (1). The volume energy density (VED), E_v, is another parameter which accounts for the combined effect of laser power and speed in addition to the hatch distance and layer thickness [37]. E_v is described by Eq. (2). The L-PBF parameters were optimized in a way that the volume energy density remained about the same for both laser powers.

$$E_l = \frac{P}{v} \tag{1}$$

$$E_v = \frac{P}{v.h.t} \tag{2}$$

Where P is the laser power, v is the laser scanning speed, t is the layer thickness, and h is the hatch distance. Note that t and h are in mm.

The laser beams for 250 W and 950 W laser powers were 80 μm diameter with Gaussian distribution and 100 μm diameter with flat top distributions respectively. It is known that large and homogenous beams are beneficial for suppressing the spatters and powder bed degradation and allowing the production of denser parts [38]. In addition, the hatch distances of the low and high laser power categories were different which can influence the final textures of the AM parts [39]. Table 1 summarizes the process parameters which were optimized and used in this study to produce different parts.

Two categories of specimens denoted as Non-graded (NG) and Graded (G) samples were manufactured (see Fig. 1). One constant laser power was employed during the whole manufacturing process in the former group while there was a transition of the laser power from 250 W

Table 1
L-PBF process parameters used in this study.

Build direction	P [W]	V [mm/s]	h [mm]	t [mm]	Beam diameter [μm]	Beam distribution	E_l [J/mm]	E_v [J/mm^3]
H	250	700	0.12	0.05	80	Gaussian	0.36	59.5
H	950	320	0.5	0.1	100	Flat top	2.97	59.4
V	950	320	0.5	0.1	100	Flat top	2.97	59.4

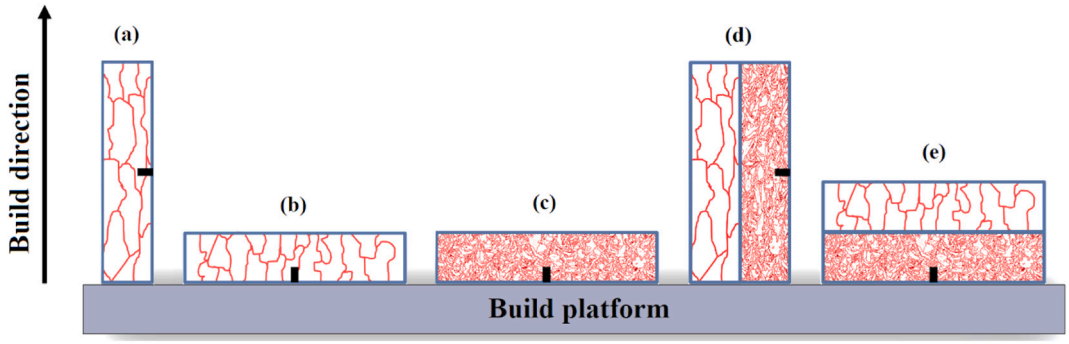

Fig. 1. Schematics of the graded and non-graded specimens showing the sample orientations with respect to the BD. Note that the crack direction (CD) is always aligned with the sample symmetry axes. (a) NG-V-950 W, (b) NG-H-950 W, (c) NG-H-250 W, (d) G-V, and (e) G-H. Note that the dimensions are schematic and not up to the actual scale.

to 950 W in the latter one. Another parameter which was altered during the manufacturing process was the building direction with respect to the sample axis or the crack direction (CD). All fatigue samples were designed in a way that the anticipated crack path was located aligned with the sample's vertical symmetry axis. The samples were denoted as vertical (V) when the build direction and CD were perpendicular, and horizontal (H) when those two directions were parallel. Graded samples and higher laser power of NG specimens, i.e. 950 W, were designed and built in two V and H orientations, while the NG 250 W samples were manufactured only in the H direction. Fig. 2 depicts a schematic of the manufactured samples showing their orientation concerning the build direction and sample axes.

Rectangular single-edge-notched samples were manufactured based on the ASTM E399 [40] specifications, as shown in Fig. 2. The final dimensions of the samples were achieved after milling. The notch with a total depth of 0.5 mm and a radius of 0.2 mm was machined using the electrical discharge machining (EDM) technique. A crack of length 1.5 mm was produced by fatigue pre-cracking in all samples according to the requirements in ASTM E399 [40].

2.2. Microstructural characterization

Optical and scanning electron microscopy (SEM) observations were performed to study the grain morphology and size, melt pools, different structures caused by various manufacturing parameters, precipitates, and carbides. Prior to the observations, samples' surfaces were prepared by grinding (180 to 2000 European grit size), polishing down to 1 μm, and etching for 3 s in a Glyceregia etchant solution of 5 ml HNO_3, 10 ml Glycerol, and 15 ml HCl. Leica DMLM optical microscope equipped with analySIS 5.0 by Olympus soft Imaging Solutions GmbH, Keyence VHX-5000, and JEOL JSM IT−100 SEM with JEOL InTouchScope software were used. Besides, fracture surface analyses by SEM were performed on the graded samples, which were intentionally overloaded in constant ΔK tests.

To identify the present phases, X-ray diffraction (XRD) analyses were performed on the wrought and non-graded samples. Prior to the XRD measurements, samples were polished for 10 min by colloidal silica. A Bruker D8 advanced diffractometer with a Co Kα radiation (wavelength of 1.78897 Å) equipped with Bruker software Diffrac. EVA vs 5.0 was used to collect the XRD patterns. The 2θ range of scan was set between 20 and 140 degrees with a scanning step size of 0.035 degrees. The X-ray beam was collimated to a spot size of 0.5 mm in diameter. The applied voltage and current were 45 kV and 35 mA respectively, which resulted in a penetration depth of 6 μm.

Crystallographic maps of the wrought and additively manufactured parts were collected using the electron backscattered diffraction (EBSD) technique to study the texture and reveal the microstructure at the surface along the fatigue crack path. Sample preparation was done

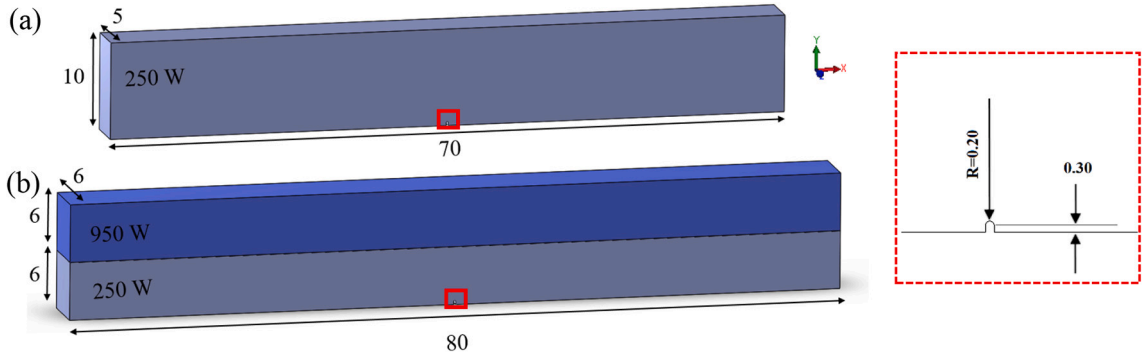

Fig. 2. The geometry of the single edge notched samples used in this study (a) non-graded and (b) graded fatigue test specimens. As provided in the text, the dimensions are slightly different for G and NG samples. The notch specifications are provided in the insert. All dimensions are in mm.

similar to the microscopy sample preparation. However, an additional polishing step with 0.25 μm colloidal silica slurry followed by ultrasonic bath cleaning with isopropanol was done. EBSD data collection was performed using an SEM Mira 3 Tescan equipped with channel 5- HKL software. The accelerating voltage was set to 20 kV. To study the crack growth path and reveal the microstructure of the materials, the step sizes of 1 μm and 0.8–1.2 μm were used for imaging around the crack and on large areas far from the cracks respectively. To post process the acquired data, TSL-OIM analysis software version 8 was used. The number of collected data points in the IPF maps used for microstructural analyses, varied from 2,797,299 points, in the scans with larger step size, to 6,842,364 points in the scan with the smallest step size. At least 96.57% of the collected points were indexed, and the lowest average confidence index (CI) of the measured data was 0.35. Grains were classified in relation to the neighboring groups as groupings of more than 10 pixels with crystallographic misorientation of larger than 5 degrees [41]. To plot the pole figures, a generalized spherical harmonic expansion smoothing with series rank (L) of 16, a Gaussian half-width of 5 degrees, and a triclinic symmetry was used.

Vickers hardness measurements were done on different AM and wrought samples using a Struers DuraScan G5 testing machine at a load of 1000 gf (HV1) and the holding time of 10 s. Hardness measurements of the NG and wrought samples were repeated 10 times to assure the reliability and consistency of the tests. For G specimens Vickers hardness measurements were performed in intervals of 0.3 mm along the entire width in multiple locations to understand the effect of the microstructure gradient on the surface hardness. Prior to the measurements, all samples surfaces were prepared as provided in the ASTM E92 [42].

2.3. Fatigue crack propagation

2.3.1. Fatigue testing

Three-point bending fatigue tests were performed using a servo hydraulic MTS machine with a loading capacity of 25 kN equipped with the MTS MultiPurpose TestWare and Flextest electronic control unit. Specifically for this work, a novel fatigue test setup, as shown in Fig. 3, capable of investigating the fatigue crack growth of graded materials in an accurate and reproducible manner, was developed. Three-point bending tests were conducted employing fatigue test configurations and stress intensity solutions as described in ASTM E399 [40]. An S690 steel platform with two fixed rollers was made and mounted to the lower grip of the MTS machine. Reference marks, with 0.5 mm intervals, were fabricated on the surface of the samples from the edge of the notch up to 7 mm. For visual crack calibration and to monitor the symmetry of the crack propagation, Limess digital image correlation (DIC) 5 megapixel cameras on two sides of the samples were used, and the average optically-measured crack lengths were periodically compared. Direct current potential drop (DCPD) equipment from Howden brand with a typical crack length measurement resolution of about 0.05 mm, was used to determine the dependence between the actual crack length and the measured voltage in two places across the samples. A polymer clamp system (PMMA) was designed to facilitate stable connections of the DCPD probes as well as to ensure the proper alignment of the samples on the platform. To minimize the errors and increase the accuracy, prior to the tests equipment and setups were tuned and calibrated.

Fatigue crack propagation testing was done through the following procedures:

- Constant K_{max} tests were done to determine the threshold stress intensity range (ΔK_{th}). The ΔK_{th} tests were conducted at a frequency of 30 Hz and an initial load ratio of $R = 0.1$ (where $R = K_{min}/K_{max}$), which then was increased to $R = 0.6$ and $R = 0.7$ for the wrought and L-PBF materials, respectively. The K_{max} was calculated according to Eq. (3) to facilitate an appropriate ΔK to grow a crack. The value of K_{min} was adjusted using Eq. (4).

$$K_{max} = \frac{\Delta K}{1 - R} \tag{3}$$

$$K_{min} = K_0 exp(C(a - a_0)) \tag{4}$$

Where K_0 is the value of the initial K_{min}, C is the stress intensity gradient which was chosen to be $-0.4\ mm^{-1}$, a_0 is the initial crack length measured optically, and a is the instantaneous crack length measured by DCPD and validated by periodical optical and DIC observations.

K_{min} was calculated and adjusted at intervals of 0.1 mm. The adjustment process was carried out until the crack did not grow by 0.1 mm in 100,000 cycles, which indicates a crack growth rate of 10^{-6} mm/cycle or less. The final reading of ΔK was considered as the ΔK_{th} value.

- Constant load amplitude tests (Paris regime) were performed to formulate the crack growth rate as a function of stress intensity range (ΔK). The crack growth rate tests were done at a frequency of 50 Hz and based on the condition provided by ASTM-E647 [43].
- The graded samples were examined under constant stress intensity range (constant ΔK) condition to evaluate the effect of the FGM microstructure on the crack growth rate behaviour. Since at a given ΔK level the FCGR is a constant value for a particular microstructure, maintaining a constant ΔK should reveal the effect of the functionally graded structure on the FCGR. It should be pointed out that the standard K solutions for determining the load levels as a function of $f(a/W)$ are for homogenous materials hence do not apply to the functionally graded parts and require adaptation.

It should be mentioned that for the constant K_{max} and constant ΔK

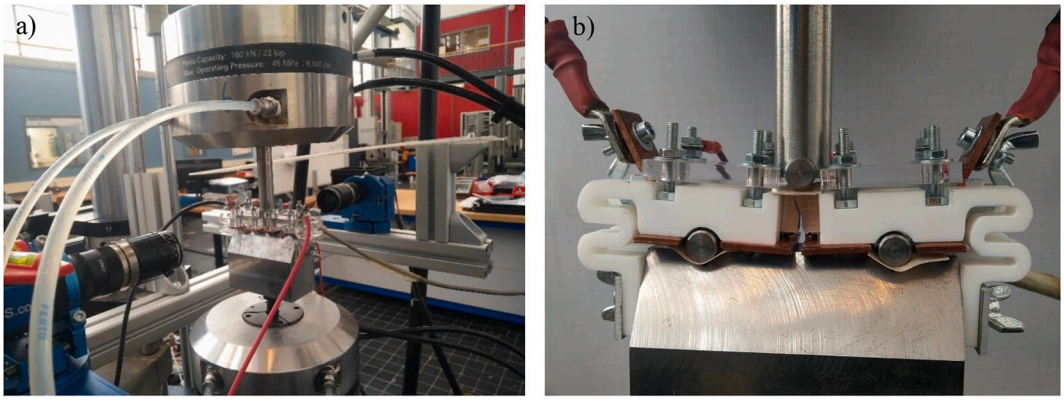

Fig. 3. The novel fatigue test setup designed for this study to facilitate accurate testing of the graded samples. (a) shows an overall view of the three-point bending test setup and equipment and (b) depicts the sample, DCPD connections, and loading fixture.

tests, the loads were adjusted automatically during crack growth, to match the desired stress intensity range for the crack length measured by the DCDP system.

2.3.2. Modelling

In order to obtain accurate customized K solutions for constant ΔK tests of graded materials, an elastic FEM model within ABAQUS software was developed. In this model, each graded specimen is represented by two halves, i.e. 250 W and 950 W, with an interface plane perpendicular to the crack. Fig. 4(a) shows the model used in the current study. The half-span of the specimen is modeled under 2D plane strain condition, where the global X axis is the transversal direction and the global Y axis is the direction of deflection. Crack is modeled at the symmetry plane of the specimen. The crack length is varied from 1.5 mm to 7.5 mm in order to study the change of the stress intensity factor during the crack growth. At the symmetry plane, displacement along X axis is constrained at the non-cracked edge, while free boundary condition is applied to the crack. The applied load is modeled with a point load along the negative Y direction at the top edge and the support is modeled as a point pined constraint at the bottom edge. Due to the symmetry, the total load applied to the FEM is 5 kN, as the test load at the mid-span of the specimen is 10 kN. The Young's moduli of the 250 W and 950 W parts are obtained from the compliance measurements of the fatigue tests of the non-graded specimens. The Poisson's ratio is set to be 0.3. The interface based on a previous research [24] has a total thickness of 1 mm and is divided into 5 layers of 0.2 mm height, with a linearly changing Young's modulus assigned to each layer. Small mesh elements of 0.02 mm are used near the crack tip, while elements of 0.5 mm are used outside the crack-influenced area. In total 185 CPE6M (6-node modified quadratic plane strain element, with hourglass control) and 4456 CPE8R (8-node biquadratic plane strain element with reduced integration) elements are used. J integral is calculated at the fifth contour from the crack tip. The fifth contour involves a circular area with a radius of 0.08 mm, shown in Fig. 4(b). K solution is then obtained from the J integral according to Eq. (5).

$$K = \sqrt{J \times \frac{E}{1-\nu^2}} \tag{5}$$

Where E is the Young's modulus at the crack tip, J is the integral value and ν is the Poisson's ratio.

The goal of conducting the constant K tests was to determine the effect of the graded microstructure on the crack growth rate. For a particular microstructure, at a given level of ΔK, the crack growth rate is expected to be constant. To maintain the constant ΔK criterion the load level should be modified based on accurate solutions of K. The standard K solutions are only applicable to materials with a constant Young's modulus (E). However, graded samples are intentionally manufactured with various microstructures, hence different material properties (including E) are expected. Therefore, prior to the FEM modelling, the values of E for the non-graded materials were estimated from the load-line-compliance [44]. The load line displacement (δ_{total}) of the fatigue test and the load line displacement in the absence of the crack, $\delta_{no\text{-}crack}$, are given by Eqs. (6) and (7) respectively.

$$\delta_{total} = \delta_{crack} + \delta_{no-crack} \tag{6}$$

$$\delta_{no-crack} = \frac{P.S^3}{4.E.B.W^3} \tag{7}$$

Where P is the applied load, S is the span length, E is the Young's modulus at the crack tip, B is the height of the sample, and W is the width of the specimen. The additional displacement due to the presence of a crack, δ_{crack} is given by Eq. (8).

$$\delta_{crack} = \frac{3.P.S^2(1-\nu^2)}{2.E.B.W^2} f\left(\frac{a}{W}\right) \tag{8}$$

Where ν is the Poisson's ratio and $f(a/W)$ is a dimensionless geometry factor defined by Eq. (9).

$$f\left(\frac{a}{W}\right) = \left(\frac{\frac{a}{W}}{1-\frac{a}{W}}\right)^2 \left\{5.58 - 19.57\left(\frac{a}{W}\right) + 36.82\left(\frac{a}{W}\right)^2 - 34.94\left(\frac{a}{W}\right)^3 + 12.77\left(\frac{a}{W}\right)^4\right\} \tag{9}$$

Measurements of displacement and load during the fatigue tests were applied to the Eqs. (6)–(9) to estimate the Young's modulus for each microstructure of AP IN718. The calculated values of Young's moduli from non-graded specimens, given in Table 2, which are in good agreement with values in [24], were applied to the FEM-model of the graded specimens to calculate the modified K solutions.

3. Results and discussions

3.1. Microstructural characterization

Fig. 5 shows the light optical microscopy images of the longitudinal cross sections of the IN718 samples processed using 250 W and 950 W

Table 2
Young's modulus of non-graded L-PBF IN718 superalloy obtained from three point bending tests.

Laser power [W]	Specimen direction	Measured Young's modulus [GPa]
950	V	139 ± 36
950	H	136 ± 10
250	H	186 ± 15

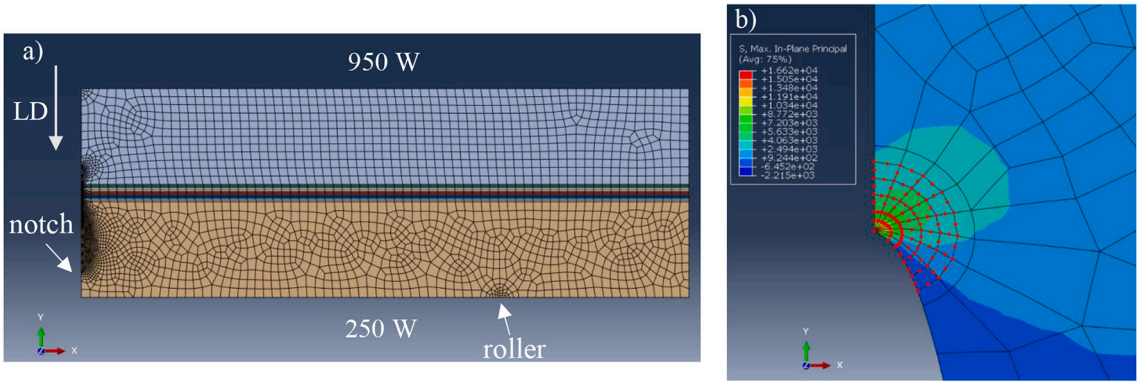

Fig. 4. a) The model used for the FEM analysis of the graded materials. Since the sample is symmetric about the axis containing the notch, half of it is modeled. The loading direction (LD) and the location of one of the rollers are determined in the figure. The notch is on the left edge where the mesh has more elements. The mid-height region which has different colours represents the five layers of the interface in the model. b) Nodes involved in the fifth contour to calculate the J integral.

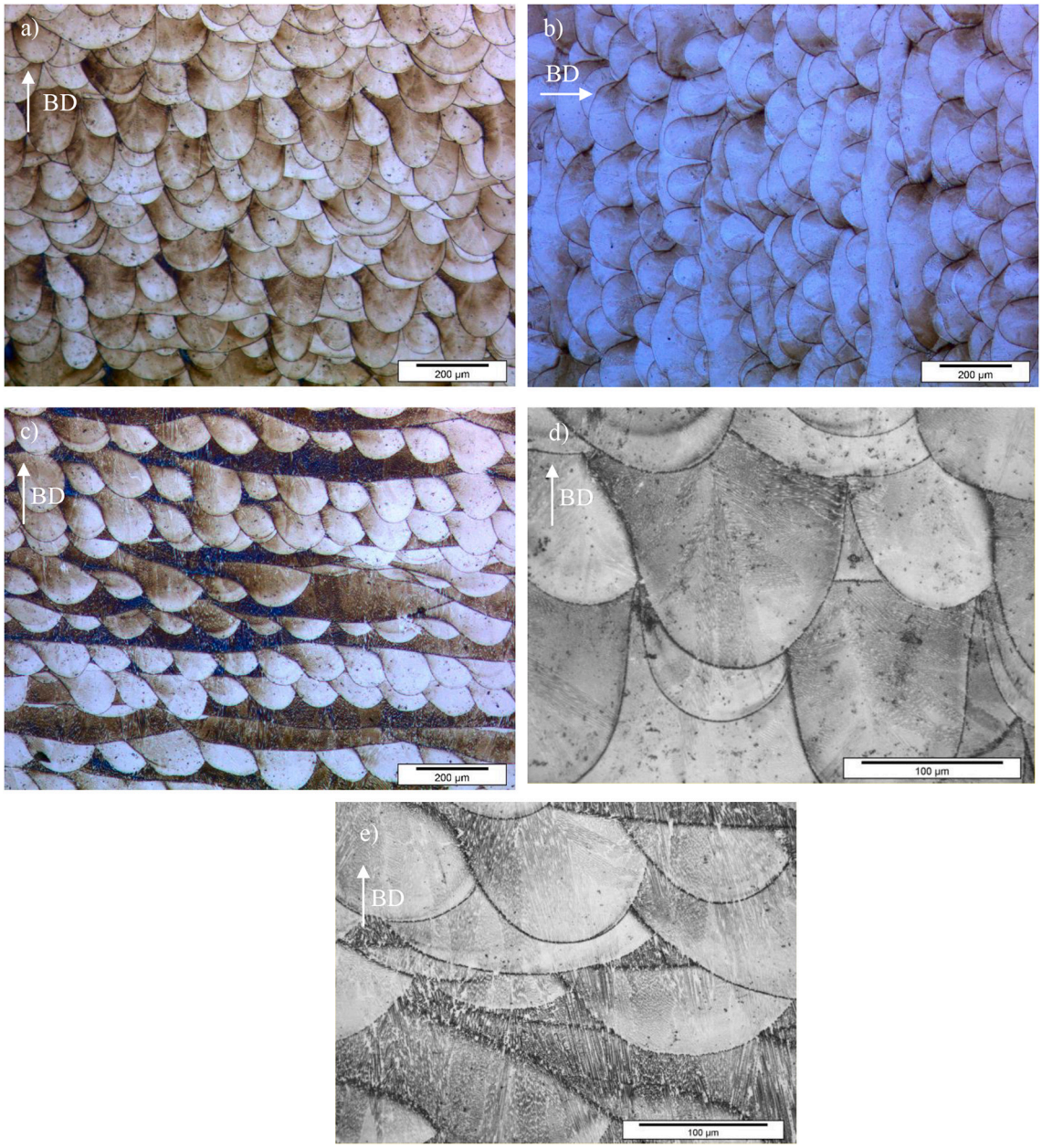

Fig. 5. Optical micrographs of longitudinal cross sections of the as-printed samples (a) 250 W-H, (b) 950 W-V, and (c) 950 W-H showing the melt pools. Higher magnification optical micrographs of (a) and (c) are provided in (d) and (e) respectively.

laser powers. Fig. 5 (a) depicts the 250 W material with finer melt pools, while Fig. 5 (b) and (c) show the 950 W material with irregular and larger melt pool contours. Moreover, higher magnification optical micrographs in Fig. 5 (d) and (e) are provided for a better comparison. The differences in the size and shape of the melt pools arise from the different process parameters used in this study. Higher laser power is capable of penetrating deeper and melting the previously solidified layers, and as a result, larger melt pools can be generated. The other parameter that affected the melt pools' size was the laser scanning speed which was 320 mm/s and 700 mm/s for the higher and lower laser powers. The lower laser scanning speed was found to result in wider and deeper melt pools and vice versa due to the changes in the melt pool penetration depth [45,46]. Considering the effect of the laser power and laser scanning speed simultaneously, lower LED values results in deeper and narrower beads, with an average of 133 µm depth and 108 µm width of the beads, while the higher LED values make shallower and wider beads, with average values of 62 µm depth and 116 µm width of the beads. Similar behaviour is reported in a previous research [47].

Optical micrographs of the longitudinal cross sections of the interfaces in the graded samples are provided in Fig. 6. The deposition of each layer in the vertical (V) sample shown in Fig. 6(a) contains a transition at the interface from 250 W to 950 W. The melt pools out of the interface region show the characteristics of the NG samples corresponding to each laser power, as discussed before. The interface is distinguished by the finer melt pools in the centre, and keyhole-induced porosities, unmelted particles, and deeper melt pools in the edges which can be a result of overlapped melt pools. In addition, the time window associated with the change of the depositing parameters which takes place in each pass can influence the interface microstructure. The transition in the horizontal (H) graded sample was smoother since each layer was deposited using one laser power, namely 250 W in the bottom of the micrograph and 950 W in the top layers, as shown in Fig. 6(b). Melt pools in the lower and upper parts are thus similar to those discussed earlier in the NG 250 W and 950 W laser power samples. Fig. 6(c)

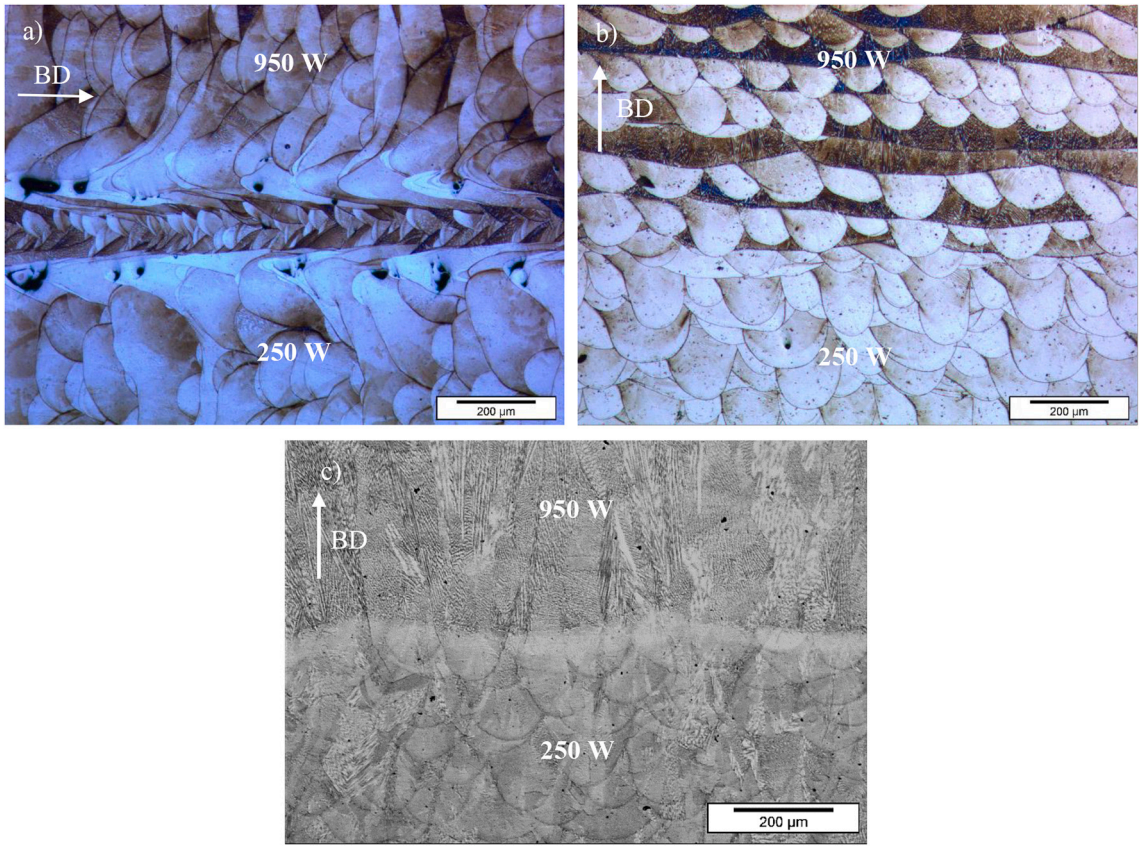

Fig. 6. Optical micrographs of the interface area in the graded AP samples in (a) V, (b), and (c) H orientations. The laser power used for each side of the interface along with the build directions are provided in the figures. It should be noted that figure c is taken by a different microscope to highlight the epitaxial columnar dendrites and interface transition.

which is also obtained on an H sample is taken by a non-digital microscope and shows the characteristic dendritic growth and epitaxial microstructure.

Fig. 7 shows the SEM micrographs of the as-processed (AP) L-PBF specimens in the sections parallel to the build direction (BD) along with a micrograph of the wrought sample. As can be seen in all L-PBF categories, grains are extended along the BD. The layer thickness of the 250 W and 950 W laser power samples were 50 µm and 100 µm, respectively. In the micrographs, the larger axis of the grains in all categories exceeds the layer thickness, which is an indication of melting the previously solidified layers and a strong trend of the epitaxial grain growth from one layer to another [24]. In the higher magnification micrographs, fine dendritic segregations are captured along the build direction. The presence of such dendritic structures has been reported in the AM IN718 alloy in the earlier research and is attributed to the very high solidification cooling rates [48,49]. Similar to the grains, dendritic structures showed the epitaxial growth between the layers in all three studied categories. To better reveal the existing larger phases such as Laves phase and carbides, the backscattered electron composition (BEC) technique was used, and imaging was performed in higher magnification. As can be seen in Fig. 7(d), carbides and inter-dendritic Laves phases are present in the AP material, which could affect the fatigue properties. The composition of these phases acquired by Energy Dispersive X-Ray Spectroscopy (EDS) is given in Table 3. In the micrograph of the wrought material shown in Fig. 7(e), needle shape and globular δ phases are captured close to the grain boundaries. Since the SEM micrographs shown in Fig. 7 are performed in such a magnification that a number of melt pools were captured, the precipitates in orders of microns could be detected. Moreover, the strengthening precipitates of the AM IN718 estimated to have their sizes ranging between 10 nm and 50 nm [50]. Therefore, compared with SEM, transmission electron microscopy (TEM) is a more suitable method for detecting them. It should be noted that the Laves phases, which form during the solidification in the AM process, are not present in the wrought material.

To identify all existing phases, XRD analyses on all groups of materials were performed and the results are summarized in Fig. 8. The precipitate peaks in the L-PBF samples are minor, and the precipitate concentration based on the previous study [24] does not exceed 2 wt%, which is not high enough to have a strong effect on the mechanical properties. In both laser powers materials, Laves phases are present, which are detrimental to the mechanical properties and can be altered by heat treatment and post processing procedures [7]. In all materials, the γ peaks were found at 2θ of 51, 59, and 89 degrees. The γ peaks at 2θ equal to 51 and 59 degrees in the 950 W- H material are not identical and the first peak is significantly shorter than the other, which suggests an anisotropy in the texture. However, the γ peaks of the 250 W and 950 W- V materials are similar, which indicates more uniform textures. The γ', γ", and δ phases peaks only were observed in the wrought materials.

The average values of the Vickers hardness in all non-graded L-PBF categories as well as the wrought material are summarized in Table 4. The average hardness values of the AM parts are relatively close to each other, with the 250 W sample category about 9% and 18% higher than the 950 W- H and 950 W- V groups. This higher hardness of the 250 W samples can be attributed to its finer grains and higher yield strength [24], which is explained by the Hall-Petch relationship. Among the two groups of 950 W laser power, the average hardness of the horizontal orientation specimens is about 11% higher than the vertical direction samples, which cannot be explained by the grain size effect. The morphology and content of the brittle Laves phases which form in the interdendritic regions [51,52] can also influence the hardness.

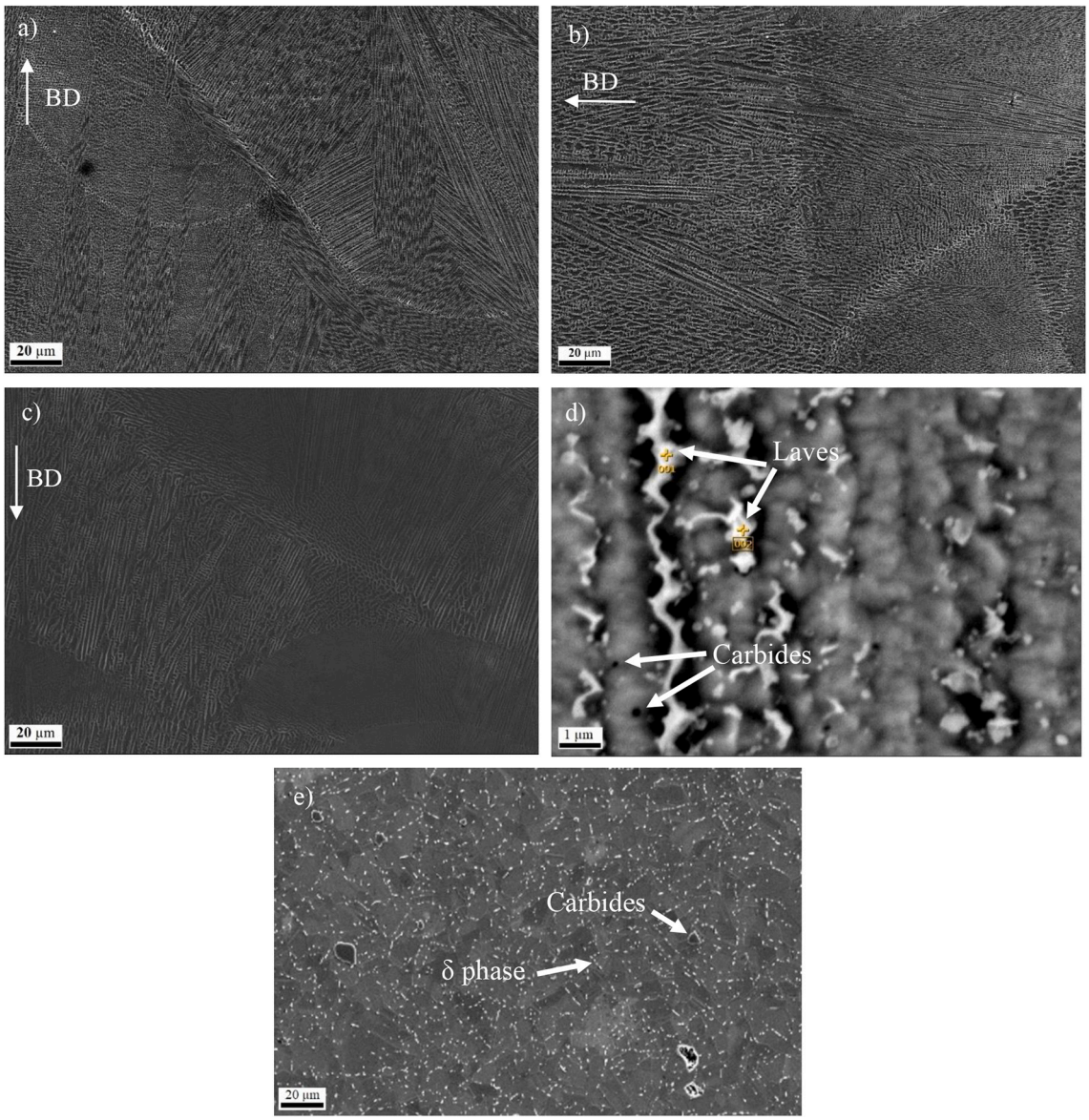

Fig. 7. SEM micrographs of the AP specimens manufactured in different conditions (a) 250 W, (b) 950 W-V, (c) 950 W-H, and (d) a high magnification BEC micrograph of the sample shown in (c). The micrograph in (e) shows an SEM image of the heat treated wrought sample where the precipitates are found mostly around the grain boundaries.

Table 3
EDS analyses of the Laves phase and carbides in the 950 W-H material.

	Ti	Cr	Mo	Fe	Ni	Nb	C
Laves	2.63	18.58	4.48	16.57	38.19	19.55	–
Carbides	7.10	0.63	–	0.57	1.37	50.19	40.15

Coarsened Laves phases with lower volume fraction result in a higher hardness compared with a higher volume fraction of fine dendrites and particles of Laves phases [51]. The Vickers hardness of the wrought material is 25% higher than that of the 250 W group. As next it will be explored in more depth, the wrought material has significantly finer grains compared with the L-PBF parts. This can result in higher yield strength and hardness. In addition, the presence of the strengthening precipitates formed during the heat treatment affects the hardness. Therefore, the higher hardness values of the wrought material arise from the combined effect of the grain size and strengthening precipitates.

Fig. 9 shows the hardness profile measured along the width of the graded samples. The measurements were done on multiple locations for both samples which are shown on the schematics provided in the insert of Fig. 9. In the V samples, the average hardness value of the material closer to the build platform, denoted as V-1, found to be a constant value of about 340 HV with some fluctuations of around 5% present due to the inhomogeneity in the microstructure [51]. Similarly, the measurements on the side further from the build platform, V-2, which correspond to the final layers of deposition, showed a constant value of about 320 HV. While the average hardness values of the V sample remain approximately constant in one layer (or close layers) of deposited material, it depends on the measurement location with respect to the build platform. The average hardness of the V sample in the parts close to the notch, i.e. near the centre of the specimen, and layers closer to the build platform were approximately constant and higher than the final deposited layers. This behaviour can be attributed to the higher number of thermal cycles which the initial and middle layers experience compared with the final deposited materials. The hardness measurements of the horizontal sample along the width, however, showed a different trend. The measurements were repeated at different distances with respect to the notch

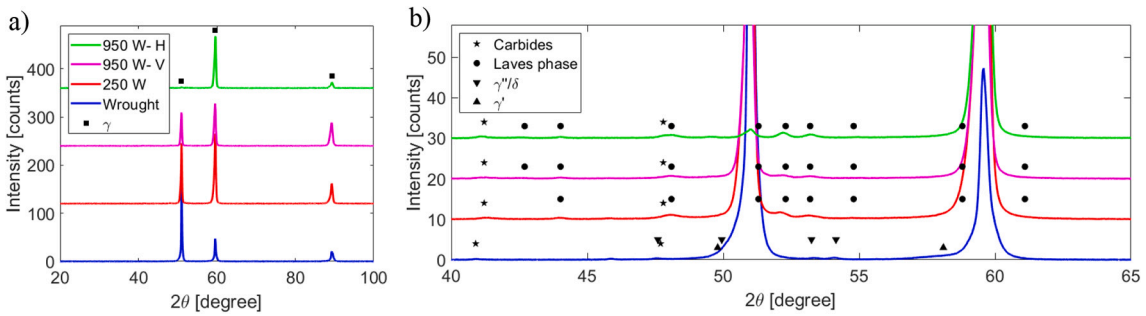

Fig. 8. XRD spectra showing different phases in the AP material manufactured using different laser powers and the wrought material. Sub-figure (b) shows a zoomed-in view with identified phases.

Table 4
Average Vickers hardness measured for different sample groups.

Sample group	Not graded					
Hardness [HV1]	H 250 W 373 ± 11	H 950 W 341 ± 9	V 950 W 303 ± 10	Wrought 486 ± 9		
	Graded					
	H 250 W side 361 ± 6	H 950 W side 340 ± 7	V 250 W side 339 ± 5	V 950 W side 340 ± 9	H Interface 351 ± 7	V Interface 341 ± 13

position. In all measurements independent of the measurement location, the average hardness value of the 250 W side, which is closer to the build platform, is about 360 HV. Going through the interface, there is no significant change of the hardness and it fluctuates between 344 HV and 358 HV. On the 950 W side, the hardness decreases to an average value of 340 HV. For a better comparison, these hardness values along with the average Vickers hardness of the non-graded and wrought material are provided in Table 4. The higher values of hardness in the layers closer to the build platform and the middle parts of the samples compared with the final deposited layers is related to the different fractions and morphology of the Laves phases which form during the last steps of solidifications. The initially deposited layers experience a larger number of thermal cycles which result in the diffusion of Nb into the matrix and decreases the Laves phase fraction [51,52]. Moving towards the final deposited layers, the material experiences fewer thermal cycles, and more Laves phase can be present, which results in a lower hardness value. The observed different behaviour in two categories of graded samples is thus a consequence of the different processing orientations. In addition, the different hardness behaviour of the V and H samples can be related to their different textures, since strong textures are known to cause anisotropy in hardness [53]. As will be discussed in the next part, horizontal samples have a strong <001> texture compared with the vertical samples. It is apparent that altering the processing parameters combined by the build direction influences the local mechanical properties. As will be shown later the observed hardness profiles for graded samples correlates well with the fatigue crack growth profiles.

To further study the effects of the manufacturing parameters on the microstructure, EBSD analyses on the planes parallel to the build directions were performed on all NG samples in addition to the heat treated wrought sample. Fig. 10 (a–d) show the Inverse Pole Figure (IPF) maps and pole figures from the EBSD analyses on the NG and wrought samples. Studied herein, L-PBF samples were found to exhibit columnar grain structures in the deposition direction. However, the grain elongations varied with the manufacturing parameters. The aspect ratio and average major axis length of the 250 W and 950 W- V are close to each other. But the 950 W- H material has significantly larger grains with a lower aspect ratio. The grains in the wrought material, are equiaxed and their size is in order of magnitude smaller than the grains in the L-PBF materials. Table 5 gives a summary of the minor and major axes lengths as well as the values of the grain aspect ratios of the NG and wrought samples. Columnar grain structures originate from the dendritic and

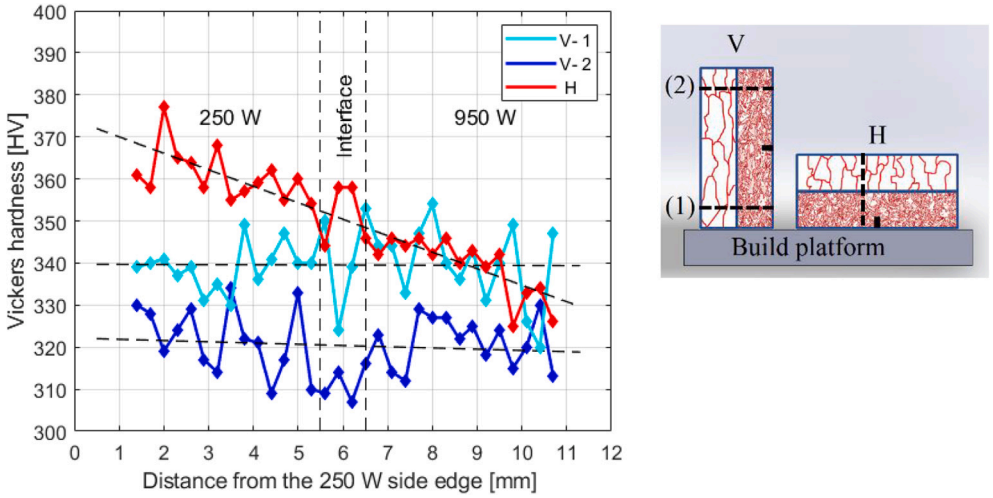

Fig. 9. Hardness profiles of AP graded samples. The measurements are done through the samples' height starting from the 250 W side. The measurements of the vertical sample are plotted for two locations: V-1 which is closer to the build platform, and V-2 which is closer to the final deposited layers. The hardness measurements were performed multiple times along with the dashed lines which are determined in the schematics provided in the insert.

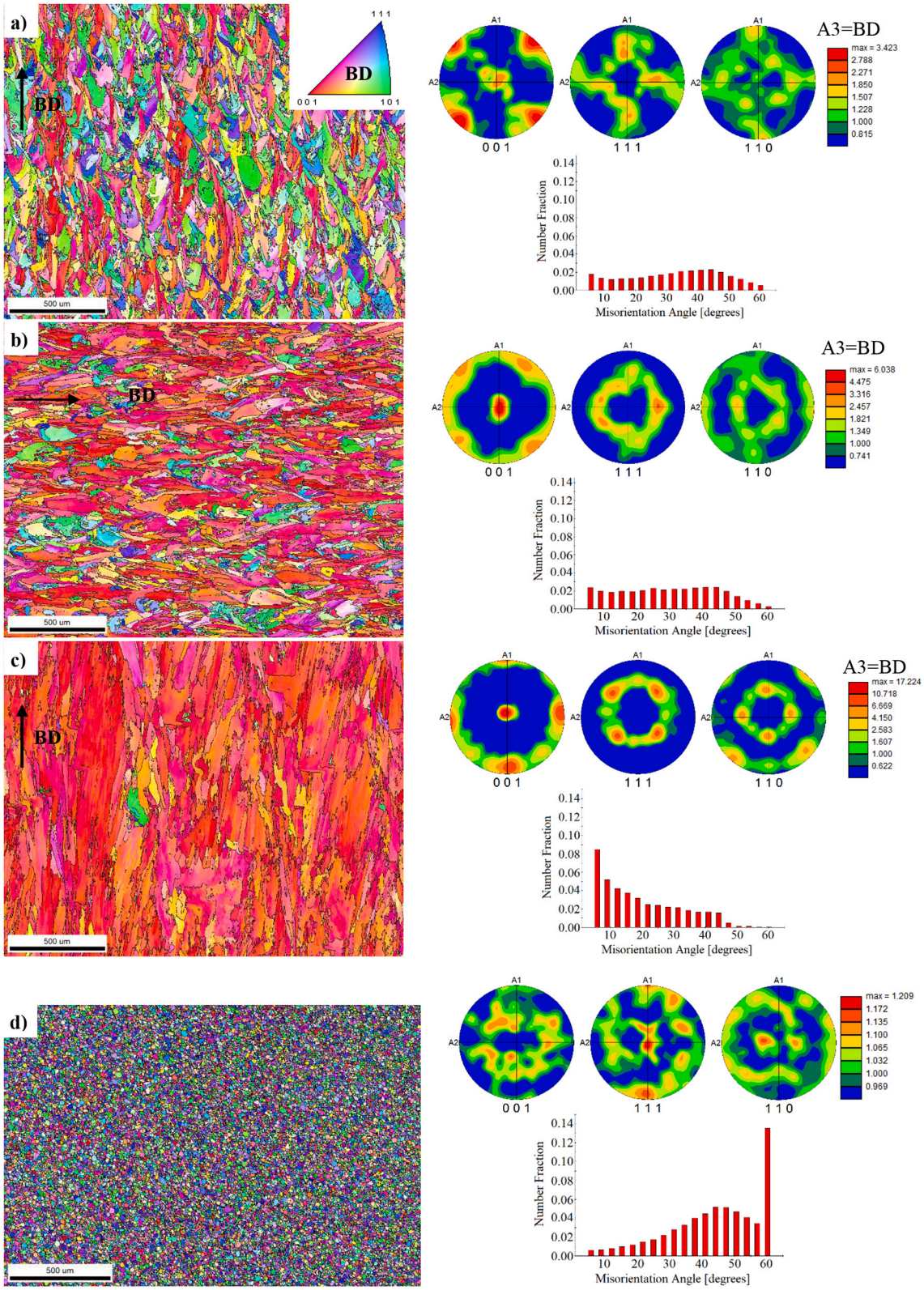

Fig. 10. Inverse pole figure maps, pole figures, and misorientation angle plots obtained from the EBSD data of L-PBF materials (a) 250 W, (b) 950 W- V, (c) 950 W- H, along with (d) wrought material. Note that grain boundaries with angles less than 5 degrees are not included in the misorientation plots. Textures of the L-PBF samples are rotated in a way that the build direction (BD) is parallel to the A3 (out of plane) direction. Intensities of the pole figures are plotted in multiples of a random distribution.

epitaxial growth, which is affected by the heat flow during the L-PBF process [24,54]. Due to the constraints imposed by the solidified parts and layers on the side and bottom, the heat flow in the molten parts is known to be perpendicular to the deposit direction and from the top to bottom [47,54]. Grains form parallel or nearly parallel to the heat flow [55]. The heat flow of different scan passes is expected to be similar and uniform in the inner parts, far enough from the sides and edges of the samples, while the heat flow of the parts closer to the edges can vary due to the effects of the free surfaces. The grain sizes can thus be influenced by this variation in the heat flow when the samples are built in different directions. It is noted that if a specific direction of an FCC crystal matches the heat flow direction of the melt pool, that particular direction will grow faster and become dominant [47]. The IPF map of the 250 W sample shows a combination of all crystallographic directions. The <001> direction is, however, dominant in the higher laser power IPF maps. In the 950 W- H sample, the faster growth of grains aligned with the <001> direction blocked the slower growing grains with other orientations.

Fig. 10 depicts the {001}, {110}, and {111} stereographic pole figures with triclinic symmetry for NG and wrought samples. The pole figures are constructed from the measured EBSD data using an orientation distribution function. The as processed AM IN718 microstructure is expected to show either cubic texture ({001}⟨100⟩) or Goss texture ({110}⟨001⟩) [56]. Fig. 10(a) gives the crystallographic texture of the 250 W sample, which shows a weak Goss texture component. Similar texture components were observed to form in the as-built AM Inconel 625 alloy [57,58]. Pole figures of the higher laser power samples are given in Fig. 10 (b) and (c). As can be seen, both 950 W-V and 950 W-H materials have strong cube textures. The largest maximum value of the multiples of a random distribution (m.r.d.) is observed in the 950 W-H material, which shows the strongest texture. The wrought sample has a weak random texture. The formation of the Goss and cube textures in different samples in this study can be attributed to the orientations of the dendritic solidifications driven by the heat flow which is controlled by the AM parameters. In addition to the various texture components, texture intensity can alter the mechanical properties in different sample categories, and thus anisotropic performance is expected.

From the misorientation angle plots of the non-graded and wrought materials in Fig. 10, it can be seen that the distribution of misorientation angles in the 250 W sample and 950 W- V specimen with finer grains are similar and more uniform, while in the horizontal samples (Fig. 10 (c)), the low angle grain boundaries (LAGB)s, i.e. misorientation angles less than 15 degrees [59], are dominant. The difference in the fraction of LAGBs could affect the fracture behaviour of these categories. High fractions of LAGBs in AM nickel-based superalloys were observed in other studies [60,61]. However, in the wrought material the presence of the annealing twin boundaries, which are defined at 60 degrees, is relatively high with a number fraction of about 0.14. Twin boundaries can increase the strength and ductility of the material by introducing more grain boundaries [62], while having detrimental effects on the fatigue performance by acting as crack nucleation sites [54,63]. The number fraction of annealing twins in the AM materials is negligible, while they are significantly present in the wrought material.

This study confirms that L-PBF parameters can be effectively used to produce and design materials with different grain size, grain shapes and orientations, textures, and grain boundary (GB) character distributions and phases. The effect of these microstructural parameters on the fatigue crack growth behaviour will further be investigated.

3.2. Fatigue crack propagation

3.2.1. FEM model

The stress intensity factors have been calculated for twenty one different crack lengths between 1.5 mm and 7.5 mm. The values of stress intensity factors were calculated from the FEM and normalized by the stress intensity factors calculated from the empirical formula given by Eq. (10) according to ISO 12135 [64].

$$f\left(\frac{a}{w}\right)=\frac{3\left(\frac{a}{w}\right)^{0.5}\left[1.99-\left(\frac{a}{w}\right)\left(1-\frac{a}{w}\right)\left(2.15-\frac{3.93a}{w}+\frac{2.7a^2}{w^2}\right)\right]}{2\left(1+\frac{2a}{w}\right)\left(1-\frac{a}{w}\right)^{1.5}} \tag{10}$$

Where a is the initial crack length, and W is the width of the specimens. The normalized values are plotted against the crack length, a, in Fig. 11. The normalized K values from the standard formula is a constant value at 1. It can be observed that the stress intensity factors of both categories of graded specimens are greater than the values calculated by the standard formula, which is due to the existence of the interface layer. The trends in both groups of G samples are very similar, with the normalized K values slightly higher for the H samples. Both curves show the most significant deviation from the standard when the crack tip is about to enter the interface. After the crack propagates across the interface, the influence of the interface vanishes. The values of the stress intensity factors reach the standard values rapidly after passing the interface.

3.2.2. Fatigue behaviour of Non-graded material

This section discusses the results of the two types of fatigue crack growth parameters, namely the stress intensity range threshold for fatigue crack growth (ΔK_{th}) and the Paris law crack growth behaviour. To

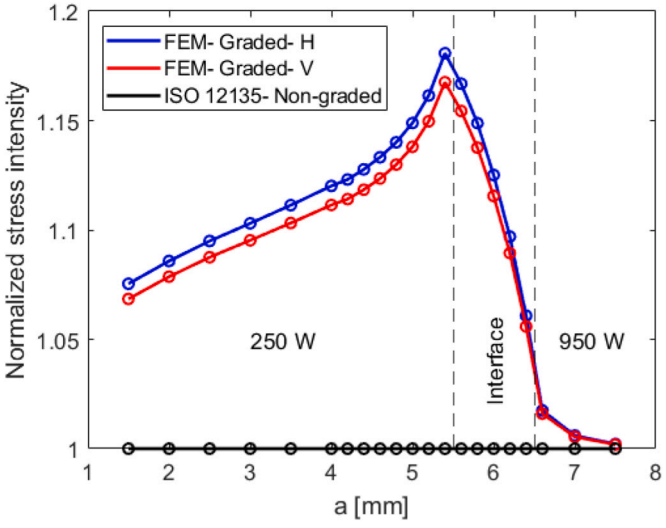

Fig. 11. Plot represents the normalized values of K versus the crack length over the width obtained from the FEM model compared with the values provided by ISO 12135 which applies to the NG materials.

Table 5
Average grain major and minor axis, aspect ratio, and grain shape of the NG IN718 as well as the wrought material.

Manufacturing condition		Major axis [μm]	Minor axis [μm]	Aspect ratio	Grain shape/preferred texture
L-PBF	250 W	135.6	28.9	0.27	Elongated in BD / no
	950 W - V	147.7	27.3	0.25	Elongated in BD / <001>
	950 W - H	518.4	79.9	0.18	Elongated in BD / <001>
Wrought		17.5	9.6	0.55	Equiaxed / no

establish the crack propagation behaviour of different microstructures, constant K_{max} tests were performed on various non-graded materials. Also, as a reference, the wrought material was tested. Table 6 gives a summary of obtained ΔK_{th} with respect to the manufacturing conditions and sample directions. In the L-PBF material categories, samples produced with 250 W laser power had the highest ΔK_{th} closely followed by the 950 W- V samples. The 950 W- H material showed the lowest amount of ΔK_{th} among the AM parts. The wrought material had a significantly higher ΔK_{th}. This behaviour can be attributed to the different microstructures in the materials. As was discussed in the previous section, the 250 W material has finer grains compared with the 950 W categories. Finer grains or more grain boundaries can introduce differently oriented less favourable slip systems, which increases the resistance to short crack growth [65]. Similarly, vertical samples with finer grains have a higher threshold stress intensity range compared with the horizontal samples with coarser grains. In addition to the smaller grains, 950 W- V samples have columnar grains oriented perpendicular to the crack direction resulting in more grain boundaries in front of the crack growth path. It should also be noted that ΔK_{th} of all produced herein L-PBF samples is twice higher than values reported for AM IN718 with the same orientations [61]. The wrought samples however showed the highest value of the threshold stress intensity range due to the equiaxed fine grains with a large number of grain boundaries in the crack path. Additionally, the presence of the strengthening precipitates formed during the heat treatment process can increase the threshold stress intensity range. In a previous research [66], ΔK_{th} of a heat treated forged IN718 (for $R = 0.1$) with grain size of 40–60 μm, was reported to be 10.2 MPa$\sqrt{m}$. This is consistent with the effect of the grain size on the ΔK_{th} and the value which was obtained in the current study.

Fig. 12 shows variations of fatigue crack growth rate against the stress intensity factor range, ΔK, describing the long crack behaviour of the various studied herein AM and wrought materials. The measured data of the L-PBF specimens showed some fluctuations, which are attributed to their heterogeneous microstructure and the residual stresses imposed during the manufacturing process [61]. It should be noted that the linear fits of the experimental data for crack growth rates of 5E-7 and higher are plotted. The fitting curves are based on the power law given by Eq. (11).

$$\frac{da}{dN} = C(\Delta K)^m \tag{11}$$

Where C is the Paris constant and m is the Paris exponent. Paris constants along with the R-squared values of the fits in Fig. 12 are summarized in Table 7.

ΔK_{th} values obtained from the curves in Fig. 12 for 250 W, H-950 W, and wrought categories are higher than those provided in Table 6, which were tested at a higher R ratio. It is known that at a low stress ratio of 0.1 the crack closure phenomenon affects the threshold stress intensity range [28,66,67]. A similar dependency of the ΔK_{th} to the stress ratio of an additively manufactured [68] and wrought [69] nickel based superalloy was reported. However, the threshold stress intensity ranges of the V-950 W L-PBF samples did not show a significant difference when R changed. In this work, a strong dependency between roughness-induced crack closure and R ratio was found for H-950 W and H-250 W L-PBF materials. Hence, threshold values reported in Table 6 can be considered as true representative values not affected by the crack closure.

Table 6
FCG threshold (ΔK_{th}) values measured in constant K_{max} tests for samples with different processing conditions.

Manufacturing condition		Sample direction	ΔK_{th} [MPa$\sqrt{m}$]	R
L-PBF	950 W	V	7.0 ± 0.3	0.7
	950 W	H	6.0 ± 0.2	0.7
	250 W	H	7.2 ± 0.3	0.7
Wrought		–	13.1 ± 0.9	0.6

As it can be seen in Fig. 12, the fatigue crack growth rate versus ΔK in 250 W and 950 W- V categories show a single fitting curve, while in the other groups, the behaviour changes around an FCGR of 1E-5. Such lower plateaus were also observed in constant K_{max} tests at $R = 0.1$ in wrought Inconel 718, which was attributed to the accumulation of fretting debris that caused darkening of the fatigue surfaces [67,69]. It is known that the larger values of the Paris exponent are indications of finer fatigue striations [61]. The wrought material and the 250 W with finer grains have higher Paris exponent values in the Paris relationship. It can be seen that for lower values of ΔK, the 250 W category has the lowest FCGR values which indicates its better fatigue performance in comparison with other specimens. For larger ΔKs in the Paris region, 950 W- V specimens show the lowest FCGR. It can be related to the larger number of grain boundaries mostly oriented perpendicular to the crack path.

3.2.3. Fatigue behaviour of graded material

The previous part focused on the fatigue behaviour of the non-graded specimens. However, one of the main interests of this study was to investigate the fatigue behaviour of the graded parts. In order to study the fatigue crack growth of the graded samples, constant ΔK tests were performed on both graded material categories. To maintain the constant ΔK condition, particularly near and across the interface area, the customized K solutions based on the J-integral values around the crack tip were used. The fatigue crack growth rate versus crack length, a, of constant ΔK experiments for both categories of graded materials are provided in Fig. 13. In both vertical and horizontal orientations, the FCGR increases as the crack propagates into the interface. This behaviour can be associated with the microstructural features of the interface area. The crack growth rate of the graded vertical 250 W➔950 W-V sample tested at 22.5 MPa$\sqrt{m}$ is relatively constant, with the variation of the $\frac{da}{dN}$ around 3E-5- 6E-5 mm/cycle in both sides of the interface. This behaviour is related to the build direction of the sample. The crack path in the V specimens grows within a layer of deposited material, which went through the same or a close number of thermal cycles. This implies that the distributions of the probable strengthening precipitates, carbides, and detrimental Laves phases are uniform along the crack path. A similar trend was observed in the Vickers hardness profile of the vertical samples, shown in Fig. 9. The crack growth rate of the vertically graded sample in the 250 W region is higher than that in the 250 W non-graded, which is about 6E-6 mm/cycle. Similarly, the FCGR of the 950 W region of the graded sample is also higher than the non-graded 950 W specimen, which is about 1E-5 mm/cycle. The differences in the $\frac{da}{dN}$ values arise from the differences in the residual stresses developed in the materials during the manufacturing process. Compressive residual stresses act as extrinsic closure factors which can lead to crack closure and hindrance of the crack growth [66]. Table 8 gives the measured residual stresses on the non-graded samples. It also should be noted that the lowest fatigue crack growth rate of the graded vertical sample, 2E-5 mm/cycle, was observed inside the interface.

The fatigue crack growth rate of the horizontal graded sample tested at $\Delta K = 25$ MPa$\sqrt{m}$, however, increases gradually from about 4E-6 mm/cycle in the lower laser power region to about 7E-5 mm/cycle in the higher laser power region. The FCGR of the 250 W region of the graded sample at the beginning is lower than its measured value in an NG sample, 2E-5 mm/cycle. However, it reaches this value before the crack propagates to the interface. Although, the FCGR has an increasing trend as the crack grows, it remains below 1.5E-4 mm/cycle which was measured on the NG 950 W specimen. This trend is in agreement with the behaviour observed in the hardness tests (shown in Fig. 9). The initially built layers, i.e. the beginning parts of the 250 W region, experienced more thermal cycles which could reduce the presence of the detrimental Laves phases. As a result, those parts have a lower FCGR. As it gets closer to the final passes of deposited material, i.e. the last parts of the 950 W regions, the number of thermal cycles which materials

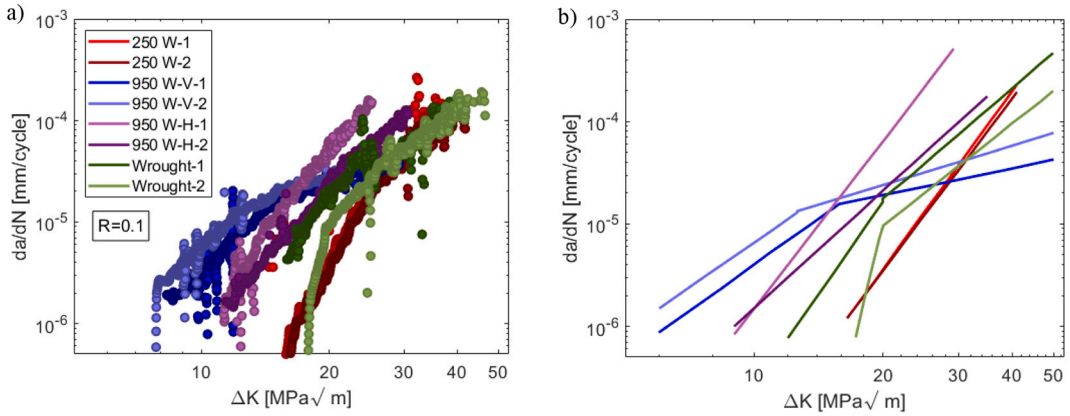

Fig. 12. (a) Measured data and (b) Paris law fits of NG L-PBF samples with different microstructures as well as the wrought samples as references. Two data sets per category are provided. The legend in (a) applies to both figures.

Table 7
A summary of Paris law constants for NG and wrought samples tested at $R = 0.1$. The ΔK_{th} values are calculated by extrapolations of the Paris curves.

Manufacturing condition		BD	ΔK_{th} [MPa$\sqrt{m}$]	Paris exponent (m_1)	Paris exponent (m_2)	Paris constant (c_1)	Paris constant (c_2)	R_1^2	R_2^2
L-PBF	950 W	V	6 ± 0.5	3.0 ± 0.1	1.1 ± 0.2	(6.0 ± 2.3) E-9	(9.4 ± 4.3) E-7	0.946	–
		H	9.2 ± 0.2	4.6 ± 0.8	–	(1.2 ± 1.1) E-10	–	0.972	0.978
	250 W	H	16.5 ± 0.1	5.7 ± 0.1	–	(1.6 ± 0.5) E-13	–	0.936	0.984
Wrought		–	15.1 ± 2.4	11.3 ± 5.7	6.1 ± 0.1	(4.5 ± 4.5) E-13	(3.5 ± 1.1) E-10	0.960	0.815

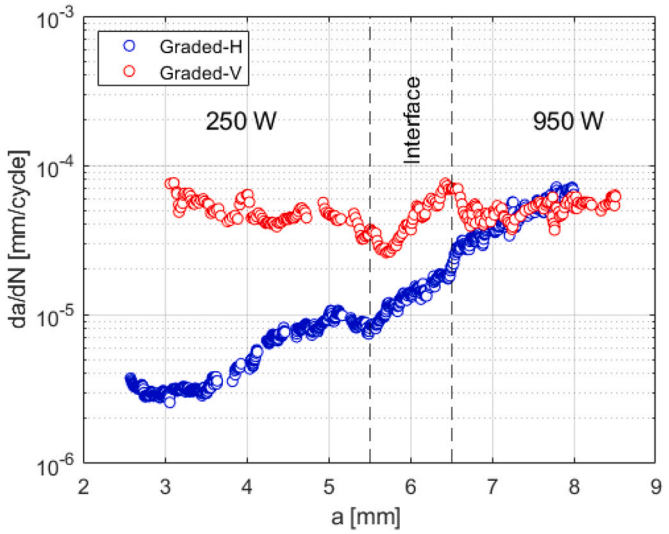

Fig. 13. Fatigue crack growth rate of the graded L-PBF samples in constant ΔK experiments.

experience reduces resulting in a larger number of Laves phase and consequently higher FCGR values. The differences in FCGR values of G and NG parts can be related to the various compressive residual strength in the NG and G parts. The interface does not influence the constant increase of the FCGR. As was observed in the optical microscopy images depicted in Fig. 6, the microstructure of the interface in the vertical graded sample was distinguishable compared with the interface of the horizontal graded sample which has a uniform and smooth transition. These differences explain the FCGR variation in the interface of the vertical G sample compared with the smooth increase of FCGR in the horizontal G specimen.

3.3. Fracture surface and crack path analyses

The fracture surface SEM micrographs of the graded samples are depicted in Fig. 14, with the interface areas determined by dashed lines. As it was observed in the optical microscopy images of the graded samples shown in Fig. 6, the vertically built specimen has more defects accumulated in the boundaries of the interface area compared with the horizontal sample. Those defects could be attributed to the change of the manufacturing parameters in each layer of the V samples around the interface area compared with the H samples in which the laser parameters remain constant in each deposited pass. To find out the type of the defects, the scanning electron microscopy was done in a higher magnification as shown in Fig. 14-c. The high magnification micrograph along with the subsequent EDS analyses revealed that the present defects are unmelted particles. The presence of these kinds of defects was reported in different additive manufactured alloys [24,29,41,70–72]. The unmelted particles can act as fatigue crack initiation sites and influence crack paths affecting the overall fatigue behaviour of AM materials dramatically [73]. In addition, the coupling of the pores between the unmelted parts with oxides and carbides hinders grain growth [29]. As it can be seen in Fig. 14 (a), the presence of the unmelted particles is more pronounced on the 250 W laser power side. In addition, the size of the unmelted particles is towards the upper limit of the particle size in the

Table 8
Residual stress values of the L-PBF IN718 samples measured by XRD technique.

Manufacturing condition		Sample direction	Residual stress in BD [MPa]	Residual stress perpendicular to BD [MPa]
L-PBF	250 W	H	−100 ± 23	−151 ± 30
	950 W	H	−368 ± 98	−259 ± 60
	950 W	V	−480 ± 66	−377 ± 44

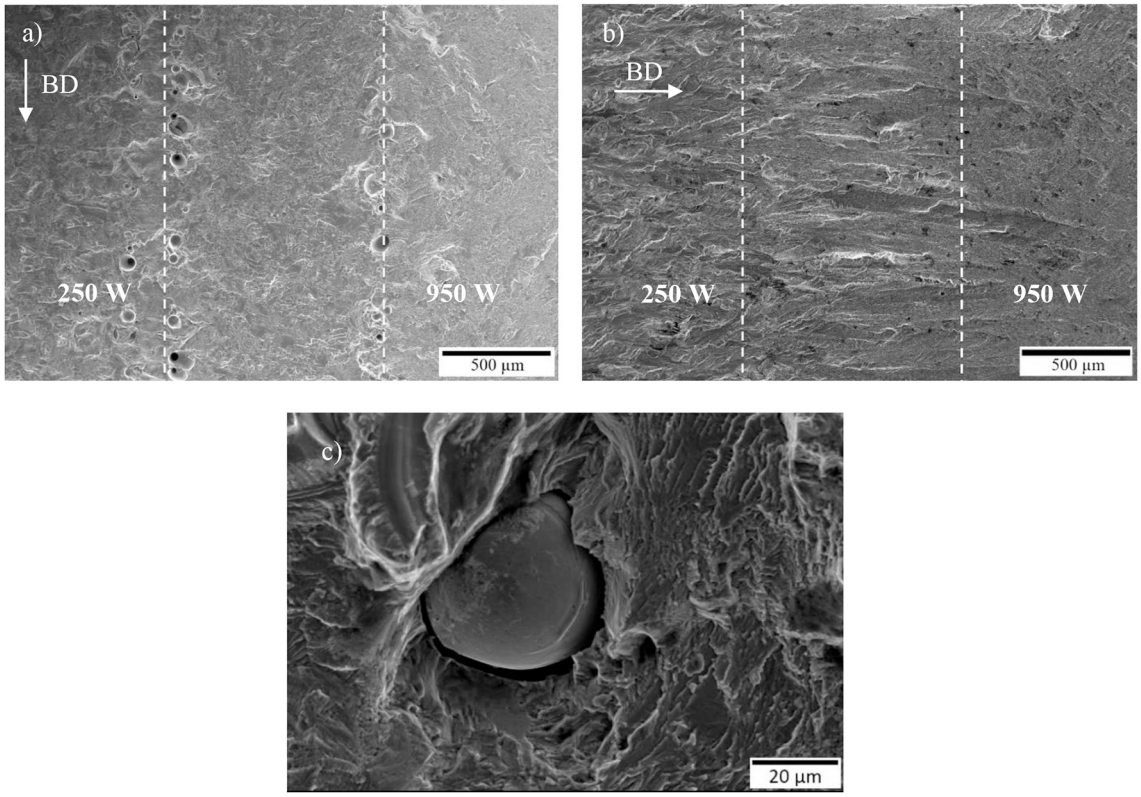

Fig. 14. SEM micrographs of the graded specimens' fractured surfaces near the interface area on (a) vertical and (b) horizontal orientations. (c) A high magnification micrograph of an un-melted particle in the interface region of the vertical specimen.

powder, 64 µm. The reason is that the 250 W laser power was not high enough to melt the larger powder particles completely, similar to what was reported in [71].

Fig. 15 shows the SEM micrographs of the fractured surface of a graded sample on the 250 W laser power region. No striations were found in the fractured surfaces, however, as seen in Fig. 15(a), stair-like features are present, which indicate the local solidification directions. These stairs are revealed after the fracture since the crack propagates through the epitaxial dendrites which were observed to grow along the <001> directions in the columnar grains. Fig. 15(b) shows a ridge on the fracture surface that can indicate the grain boundaries with different local orientations in adjacent grains or melt pool boundaries.

The optical micrographs of the crack path of a horizontal graded sample in regions manufactured using different laser powers are given in Figs. 16 (a) and (b). Note that the macroscopic crack propagation direction is from the bottom (250 W laser power) to the top. Significant deflections are observed when crack encounters the boundaries of melt pools (shown by 1 in Fig. 16 (a)) and the interface region (shown by 2 in Fig. 16(a)), resulting in a tortuous crack path. Such deflections are not present at the boundaries of the 950 W region shown in Fig. 16(b). The crack path of the wrought sample, which has significantly finer grains compared with the graded parts, is shown in 16 (c). The crack path is observed to be relatively straight, featuring a combination of transgranular and intergranular fracture.

To analyse the effect of the microstructure and grain orientations on the crack propagation behaviour of the graded and wrought materials, EBSD imaging is performed around the cracks, and the IPF maps are presented in Fig. 17 (a)–(c). The build directions of the graded specimens are indicated on the IPF maps. In all maps, the crack propagates from right to left. The grain sizes manufactured using 250 W laser power were found to be similar in both H and V graded samples and elongated in the build direction. However, similar to what was observed on the NG

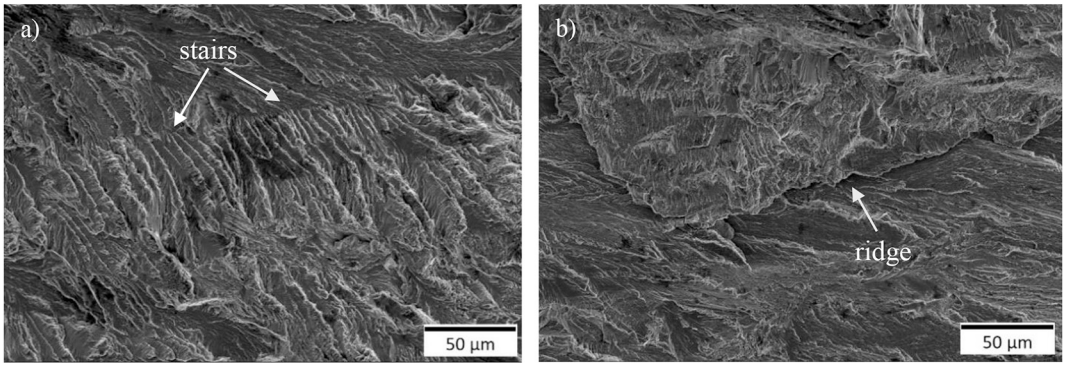

Fig. 15. SEM micrographs of the fractured surfaces of the graded samples in the regions manufactured using 250 W laser power tested at $\Delta K = 25$ MPa$\sqrt{m}$, showing (a) stair like features and (b) ridges revealing two grains.

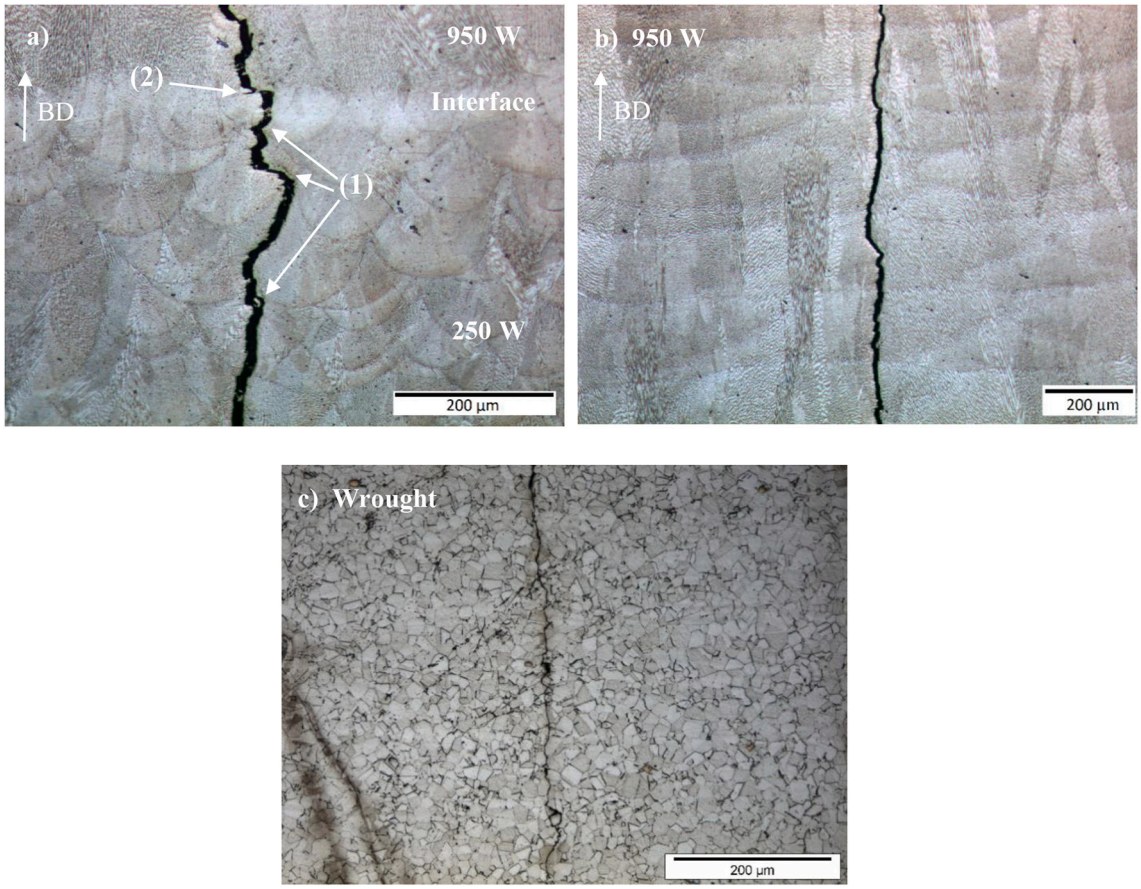

Fig. 16. Optical micrographs showing the crack path of a horizontal graded sample in the (a) 250 W laser power side and the interface, (b) 950 W laser power side, and (c) the crack path of the wrought sample. Crack deflections at melt pool boundaries (1) and interface (2) are determined in figure (a).

samples' IPFs shown in Fig. 10, in the 950 W laser power regions, the build direction influences the grain size. The 950 W side of the H graded sample was observed to have larger grains compared with the V sample. The other difference in the two orientations of the G samples is the interface region. From the optical microscopy images shown in Fig. 6, the transition from 250 W to 950 W regions in the H samples was found to be smoother compared with the V specimens. This feature is evident in the IPF maps as well. The interface microstructure is not distinguishable in the H sample, while the texture of the interface in the V sample is significantly different from the other parts. The V sample's interface margin on the 250 W side consists of finer grains and defects, which were discussed earlier and shown in the optical micrographs in Fig. 16. Similarly, on the other side of the interface, where the 950 W laser power is used, grains are finer compared with the remaining area of 950 W. The other noticeable feature of the V sample's interface is the orientations of the grains. The grains located towards the lower laser power are oriented in the <001> direction, while the other parts do not show a preferred texture. In both graded samples, deflections were observed close to the grain boundaries, similar to what was reported in a previous research [74].

From the IPF maps, it can be observed that despite having some intergranular fracture, the transgranular fatigue mechanism is dominant in the fatigue crack growth of the AP graded materials. Similar behaviour was reported in [61,75]. However, the crack grows as a combination of transgranular and intergranular in the wrought material, as was evident in the optical micrographs in Fig. 15. Crack branching (CB), which is known to form at the grain boundary high angle misorientation, was observed in the crack growth path and is determined in the IPFs. Crack branching hinders the fatigue crack growth due to the reduction of effective stress intensity factor at the crack tip [61]. The crack branching phenomenon was observed more in the H sample compared with the V specimen, and it can be related to the lower fatigue crack growth rate of the H sample. The intergranular crack growth mechanism, which was observed in V samples more than H samples, can occur when the crack tip encounters high angle grain boundaries [75].

Schematics of the crack path in the H and V samples are provided in Fig. 18. As it was observed from the optical micrographs given in Fig. 16 and the IPFs in Fig. 17, the crack deflections are larger in H samples which could be resulted from the <001> texture of the grains compared with the V samples, which show deflections around the melt pool boundaries. There are more deflections in the V samples causing a more tortuous crack path. The dominant fracture mechanism in both graded samples was observed to be transgranular due to the encounter of the crack tip to the high angle grain boundaries.

4. Conclusions

In this study, we investigated the effect of the different processing parameters in creating various microstructures and resulting hardness and fatigue behaviour of the L-PBF IN718 superalloy. In particular, the correlation of the aforementioned mechanical properties with the microstructure was studied. Three groups of non-graded specimens, along with two categories of the functionally graded samples, in which the processing parameters were used to manipulate the properties, were tested at room temperature. A heat treated wrought IN718 material was also tested as a reference for comparing the performance of the graded and non-graded materials. A finite element model was developed to obtain the accurate K solutions in the interface regions of the graded materials. Several conclusions can be drawn:

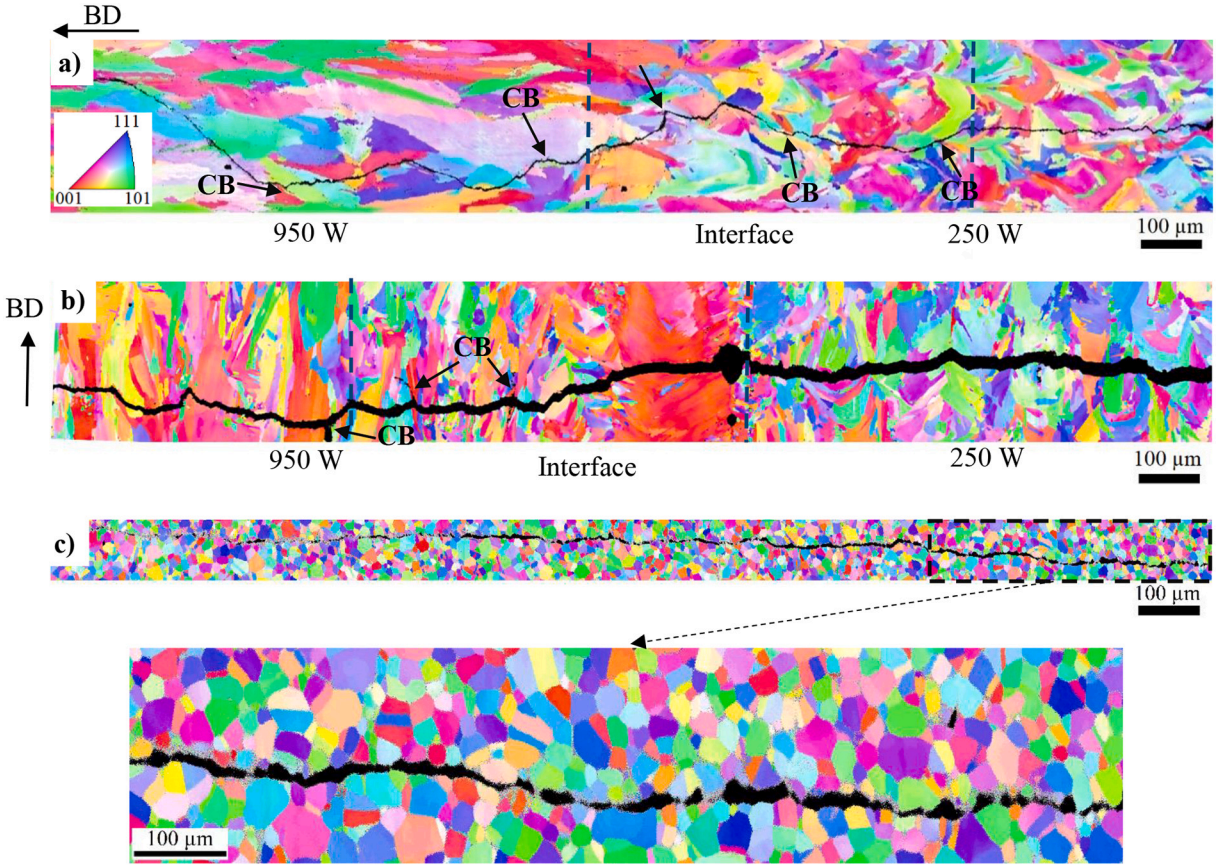

Fig. 17. IPF maps showing the crack paths through the interface of the graded samples built in (a) H and (b) V orientations tested at $\Delta K = 22.5$ MPa$\sqrt{m}$ and $\Delta K = 25$ MPa$\sqrt{m}$ respectively. The orientations of the grains with respect to the local crystal lattice frame in all IPFs are determined based on the IPF triangle presented in (a). A higher magnification IPF of the wrought sample is presented in the insert from the determined area in (c). As it can be seen the crack grows as a combination of intergranular and transgranular mechanisms.

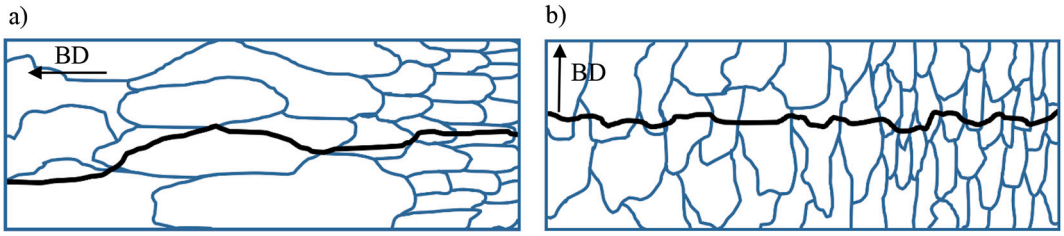

Fig. 18. A crack path schematic of (a) horizontal and (b) vertical samples.

1) *Microstructural Anisotropy:* The grains' shape and texture were found highly affected by the manufacturing parameters and build directions. The grains are elongated in the build direction and exhibit strong <001> texture, which was found to be the most pronounced in the horizontal build direction of the higher laser power. The wrought material has almost equiaxed fine grains.
2) *Hardness profile:* Non-graded L-PBF materials had uniform values of hardness, which were lower than those of the wrought material. The difference was attributed to the finer grains and the presence of the strengthening precipitates in the wrought samples. The hardness profile of the graded material was affected by the processing direction and grading type and was found to reflect well the profile of fatigue crack growth.
3) *Fatigue crack growth behaviour ($\Delta K_{th}$and da/dN) of non-graded material:* At a low stress ratio of $R = 0.1$, only 250 W L-BPF material was found to have comparable to wrought heat treated material fatigue crack growth behaviour. The 950 W category was found to exhibit in general worse than the 250 W material fatigue behaviour. This was attributed to the compressive residual stresses, leading to less ΔK_{eff} in the 250 W samples with finer grains. At higher stress ratio of $R = 0.7$, the threshold stress intensity range in AM materials decreases, which is related to the absence of the roughness-induced crack closure mechanisms observed at $R = 0.1$.
4) *Fatigue crack growth behaviour of graded material*: A novel approach of using a constant ΔK procedure was employed for graded specimens, which allows investigating the crack growth rate as a function of the crack interaction with the local microstructures. It was observed that the graded microstructures influence the *da/dN* values. While the values obtained for the low and high laser power zones were different from their ungraded counterparts, the crack growth rates were seen to be reducing as the crack path encounters the interface regions.
5) *Fatigue crack path:* Melt pool boundaries, graded interface boundaries, and grain orientations close to <001> were found to influence

and deflect the crack path. Furthermore, grain boundary misorientation was observed to cause crack branching for horizontal high laser power samples.

Thus, in this study, we have successfully demonstrated the feasibility of using an additive manufacturing process to fabricate functionally graded materials, which could feature tailorable fatigue response based on the location-specific microstructures. Future works will focus on the effects of various heat treatments on fatigue and fracture toughness behaviour of such graded materials. Furthermore, the effect of the carbides and delta phase fractions on the fatigue performance of the AM IN718 could be an interesting future study.

Data availability

The raw/processed data required to reproduce these findings cannot be shared at this time due to technical or time limitations.

Declaration of Competing Interest

The authors declare that they have no known competing financial interests or personal relationships that could have appeared to influence the work reported in this paper.

Acknowledgements

We acknowledge the support from the Russian Science Foundation grant (project No. 19–79-30002).

References

[1] M. Clavel, A. Pineau, Frequency and wave-form effects on the fatigue crack growth behavior of alloy 718 at 298 K and 823 K, Metall. Trans. A. 9 (4) (1978) 471–480.
[2] S. Ghorbanpour, M. Zecevic, A. Kumar, M. Jahedi, J. Bicknell, L. Jorgensen, I. J. Beyerlein, M. Knezevic, A crystal plasticity model incorporating the effects of precipitates in superalloys: application to tensile, compressive, and cyclic deformation of Inconel 718, Int. J. Plast. 99 (2017) 162–185.
[3] G. Nicoletto, Smooth and notch fatigue behavior of selectively laser melted Inconel 718 with as-built surfaces, Int. J. Fatigue 128 (2019) 105211.
[4] P.D. Nezhadfar, A.S. Johnson, N. Shamsaei, Fatigue behavior and microstructural evolution of additively manufactured Inconel 718 under cyclic loading at elevated temperature, Int. J. Fatigue 136 (2020) 105598.
[5] S. Ghorbanpour, M.E. Alam, N.C. Ferreri, A. Kumar, B.A. McWilliams, S.C. Vogel, J. Bicknell, I.J. Beyerlein, M. Knezevic, Experimental characterization and crystal plasticity modeling of anisotropy, tension-compression asymmetry, and texture evolution of additively manufactured Inconel 718 at room and elevated temperatures, Int. J. Plast. 125 (2020) 63–79.
[6] S. Gribbin, S. Ghorbanpour, N.C. Ferreri, J. Bicknell, I. Tsukrov, M. Knezevic, Role of grain structure, grain boundaries, crystallographic texture, precipitates, and porosity on fatigue behavior of Inconel 718 at room and elevated temperatures, Mater. Charact. 149 (2019) 184–197.
[7] E. Hosseini, V.A. Popovich, A review of mechanical properties of additively manufactured Inconel 718, Add. Manufact. 30 (2019) 100877.
[8] J.M. Oblak, D.F. Paulonis, D.S. Duvall, Coherency strengthening in Ni base alloys hardened by DO22 γ' precipitates, Metall. Trans. A. 5 (1) (1974) 143.
[9] D.F. Paulonis, J.M. Oblak, D.S. Duvall, Precipitation in nickel-base alloy 718, ASM (Amer. Soc. Metals), Trans. Quart. 62 (1969) 611–622.
[10] D.W. Worthem, I.M. Robertson, F.A. Leckie, D.F. Socie, C.J. Altstetter, Inhomogeneous deformation in INCONEL 718 during monotonic and cyclic loadings, Metallurgical transactions, A, Phys. Metal. Mater. Sci. 21 A (12) (1990) 3215–3220.
[11] L. Xiao, D.L. Chen, M.C. Chaturvedi, Shearing of γ″ precipitates and formation of planar slip bands in Inconel 718 during cyclic deformation, Scr. Mater. 52 (7) (2005) 603–607.
[12] M. Xie, N. Foundoukos, J.C. Chapman, Experimental and numerical investigation on the shear behaviour of friction-welded bar-plate connections embedded in concrete, J. Constr. Steel Res. 61 (5) (2005) 625–649.
[13] C. Wang, R. Li, Effect of double aging treatment on structure in Inconel 718 alloy, J. Mater. Sci. 39 (7) (2004) 2593–2595.
[14] N.C. Ferreri, S.C. Vogel, M. Knezevic, Determining volume fractions of γ, γ', γ″, δ, and MC-carbide phases in Inconel 718 as a function of its processing history using an advanced neutron diffraction procedure, Mater. Sci. Eng. A 781 (2020) 139228.
[15] A. Strondl, R. Fischer, G. Frommeyer, A. Schneider, Investigations of MX and γ'/γ″ precipitates in the nickel-based superalloy 718 produced by electron beam melting, Mater. Sci. Eng. A 480 (1–2) (2008) 138–147.
[16] J. Fu, M. Qiu, L. Shen, L. Kong, J. Ma, On processing of Inconel718 through multi-channel discharge ablation, J. Manuf. Process. 57 (2020) 462–468.
[17] T. Connolley, P.A.S. Reed, M.J. Starink, Short crack initiation and growth at 600°C in notched specimens of Inconel718, Mater. Sci. Eng. A 340 (1) (2003) 139–154.
[18] H. Andersson, C. Persson, In-situ SEM study of fatigue crack growth behaviour in IN718, Int. J. Fatigue 26 (3) (2004) 211–219.
[19] H. Andersson, C. Persson, T. Hansson, Crack growth in IN718 at high temperature, Int. J. Fatigue 23 (9) (2001) 817–827.
[20] L.A. James, W.J. Mills, Effect of heat-treatment upon the fatigue-crack growth behavior of alloy 718 Weldments—part I: macroscopic behavior, J. Eng. Mater. Technol. 107 (1) (1985) 34–40.
[21] G.A. Osinkolu, G. Onofrio, M. Marchionni, Fatigue crack growth in polycrystalline IN 718 superalloy, Mater. Sci. Eng. A 356 (1) (2003) 425–433.
[22] J.L. Yuen, P. Roy, Effect of grain size on the near threshold fatigue crack propagation of a nickel base precipitation hardened superalloy, Scr. Metall. 19 (1) (1985) 17–22.
[23] H. Helmer, A. Bauereiß, R.F. Singer, C. Körner, Grain structure evolution in Inconel 718 during selective electron beam melting, Mater. Sci. Eng. A 668 (2016) 180–187.
[24] V.A. Popovich, E.V. Borisov, A.A. Popovich, V.S. Sufiiarov, D.V. Masaylo, L. Alzina, Functionally graded Inconel 718 processed by additive manufacturing: crystallographic texture, anisotropy of microstructure and mechanical properties, Mater. Des. 114 (2017) 441–449.
[25] W.A. Tayon, R.N. Shenoy, M.R. Redding, R. Keith Bird, R.A. Hafley, Correlation between microstructure and mechanical properties in an Inconel 718 deposit produced via Electron beam freeform fabrication, J. Manuf. Sci. Eng. 136 (6) (2014).
[26] A. Tabei, E. Mirkoohi, H. Garmestani, S. Liang, Modeling of texture development in additive manufacturing of Ni-based superalloys, Int. J. Adv. Manuf. Technol. 103 (1) (2019) 1057–1066.
[27] E. Brandl, U. Heckenberger, V. Holzinger, D. Buchbinder, Additive manufactured AlSi10Mg samples using selective laser melting (SLM): microstructure, high cycle fatigue, and fracture behavior, Mater. Des. 34 (2012) 159–169.
[28] R. Konečná, L. Kunz, G. Nicoletto, A. Bača, Long fatigue crack growth in Inconel 718 produced by selective laser melting, Int. J. Fatigue 92 (2016) 499–506.
[29] C. Pei, D. Shi, H. Yuan, H. Li, Assessment of mechanical properties and fatigue performance of a selective laser melted nickel-base superalloy Inconel 718, Mater. Sci. Eng. A 759 (2019) 278–287.
[30] X.F. Ma, H.L. Zhai, L. Zuo, W.J. Zhang, S.S. Rui, Q.N. Han, J.S. Jiang, C.P. Li, G. F. Chen, G.A. Qian, S.J. Zhao, Fatigue short crack propagation behavior of selective laser melted Inconel 718 alloy by in-situ SEM study: influence of orientation and temperature, Int. J. Fatigue 139 (2020) 105739.
[31] A. Kawasaki, R. Watanabe, Concept and P/M fabrication of functionally gradient materials, Ceram. Int. 23 (1) (1997) 73–83.
[32] W. Meng, W. Zhang, W. Zhang, X. Yin, B. Cui, Fabrication of steel-Inconel functionally graded materials by laser melting deposition integrating with laser synchronous preheating, Opt. Laser Technol. 131 (2020) 106451.
[33] W. Liu, J.N. DuPont, Fabrication of functionally graded TiC/Ti composites by laser engineered net shaping, Scr. Mater. 48 (9) (2003) 1337–1342.
[34] V.A. Popovich, E.V. Borisov, V.S. Sufiyarov, A.A. Popovich, Tailoring the properties in functionally graded alloy inconel 718 using additive technologies, Metal Sci. Heat Treat. 60 (11) (2019) 701–709.
[35] V.A. Popovich, E.V. Borisov, V. Heurtebise, T. Riemslag, A.A. Popovich, V. S. Sufiiarov, Creep and Thermomechanical fatigue of functionally graded Inconel 718 produced by additive manufacturing, in: T.M.M. Materials Society (Ed.), TMS 2018 147th Annual Meeting & Exhibition Supplemental Proceedings, Springer International Publishing, Cham, 2018, pp. 85–97.
[36] A. 5383, Nickel Alloy, Corrosion and Heat-Resistant, Investment Castings, 52.5Ni - 19Cr - 3.0Mo - 5.1Cb(Nb) - 0.90Ti - 0.60Al - 18Fe, Vacuum Melted Homogenization and Solution Heat Treated, SAE International, 1966.
[37] J.-N. Zhu, E. Borisov, X. Liang, E. Farber, M.J.M. Hermans, V.A. Popovich, Predictive analytical modelling and experimental validation of processing maps in additive manufacturing of nitinol alloys, Add. Manufact. 38 (2021) 101802.
[38] M.C. Sow, T. De Terris, O. Castelnau, Z. Hamouche, F. Coste, R. Fabbro, P. Peyre, Influence of beam diameter on laser powder bed fusion (L-PBF) process, Add. Manufact. 36 (2020) 101532.
[39] N. Nadammal, S. Cabeza, T. Mishurova, T. Thiede, A. Kromm, C. Seyfert, L. Farahbod, C. Haberland, J.A. Schneider, P.D. Portella, G. Bruno, Effect of hatch length on the development of microstructure, texture and residual stresses in selective laser melted superalloy Inconel 718, Mater. Des. 134 (2017) 139–150.
[40] Standard Test Method for Linear-Elastic Plane-Strain Fracture Toughness of Metallic Materials.
[41] N.C. Ferreri, S. Ghorbanpour, S. Bhowmik, R. Lussier, J. Bicknell, B.M. Patterson, M. Knezevic, Effects of build orientation and heat treatment on the evolution of microstructure and mechanical properties of alloy mar-M-509 fabricated via laser powder bed fusion, Int. J. Plast. 121 (2019) 116–133.
[42] ASTM, Standard Test Methods for Vickers Hardness and Knoop Hardness of Metallic Materials, 2018.
[43] A. E647, Standard Test Method for Measurement of Fatigue Crack Growth Rates, 2000.
[44] H. Tada, P.C. Paris, G.R. Irwin, The Stress Analysis of Cracks Handbook, ASME Press, Third Edition, 2000.
[45] I. Hacısalihoğlu, F. Yıldiz, A. Çelik, The effects of build orientation and hatch spacing on mechanical properties of medical Ti–6Al–4V alloy manufactured by selective laser melting, Mater. Sci. Eng. A 802 (2021) 140649.
[46] M. Balbaa, S. Mekhiel, M. Elbestawi, J. McIsaac, On selective laser melting of Inconel 718: densification, surface roughness, and residual stresses, Mater. Des. 193 (2020) 108818.

[47] A. Keshavarzkermani, M. Sadowski, L. Ladani, Direct metal laser melting of Inconel 718: process impact on grain formation and orientation, J. Alloys Compd. 736 (2018) 297–305.
[48] S. Raghavan, B. Zhang, P. Wang, C.-N. Sun, M.L.S. Nai, T. Li, J. Wei, Effect of different heat treatments on the microstructure and mechanical properties in selective laser melted INCONEL 718 alloy, Mater. Manuf. Process. 32 (14) (2017) 1588–1595.
[49] E. Chlebus, K. Gruber, B. Kuźnicka, J. Kurzac, T. Kurzynowski, Effect of heat treatment on the microstructure and mechanical properties of Inconel 718 processed by selective laser melting, Mater. Sci. Eng. A 639 (2015) 647–655.
[50] K. Sano, N. Oono, S. Ukai, S. Hayashi, T. Inoue, S. Yamashita, T. Yoshitake, γ″-Ni3Nb precipitate in Fe–Ni base alloy, J. Nucl. Mater. 442 (1–3) (2013) 389–393.
[51] Y. Zhang, Z. Li, P. Nie, Y. Wu, Effect of precipitation on the microhardness distribution of diode laser epitaxially deposited IN718 alloy coating, J. Mater. Sci. Technol. 29 (4) (2013) 349–352.
[52] A. Segerstark, J. Andersson, L.-E. Svensson, O. Ojo, Microstructural characterization of laser metal powder deposited alloy 718, Mater. Charact. 142 (2018) 550–559.
[53] J. Chao, C. Capdevila, The influence of texture on the ductile-to-brittle transition behavior in Fe20Cr4.5Al oxide dispersion strengthened alloy, Metals 10 (1) (2020) 87.
[54] D.H. Smith, J. Bicknell, L. Jorgensen, B.M. Patterson, N.L. Cordes, I. Tsukrov, M. Knezevic, Microstructure and mechanical behavior of direct metal laser sintered Inconel alloy 718, Mater. Charact. 113 (2016) 1–9.
[55] H.L. Wei, J. Mazumder, T. DebRoy, Evolution of solidification texture during additive manufacturing, Sci. Rep. 5 (1) (2015) 16446.
[56] X. Yu, X. Lin, F. Liu, L. Wang, Y. Tang, J. Li, S. Zhang, W. Huang, Influence of post-heat-treatment on the microstructure and fracture toughness properties of Inconel 718 fabricated with laser directed energy deposition additive manufacturing, Mater. Sci. Eng. A 798 (2020) 140092.
[57] D. Ma, A.D. Stoica, Z. Wang, A.M. Beese, Crystallographic texture in an additively manufactured nickel-base superalloy, Mater. Sci. Eng. A 684 (2017) 47–53.
[58] X.Y. Fang, H.Q. Li, M. Wang, C. Li, Y.B. Guo, Characterization of texture and grain boundary character distributions of selective laser melted Inconel 625 alloy, Mater. Charact. 143 (2018) 182–190.
[59] E. Tochigi, A. Nakamura, N. Shibata, Y. Ikuhara, Dislocation structures in low-angle grain boundaries of α-Al2O3, Crystals 8 (3) (2018) 133.
[60] H. Wu, D. Zhang, B. Yang, C. Chen, Y. Li, K. Zhou, L. Jiang, R. Liu, Microstructural evolution and defect formation in a powder metallurgy nickel-based superalloy processed by selective laser melting, J. Mater. Sci. Technol. 36 (2020) 7–17.
[61] X. Yu, X. Lin, H. Tan, Y. Hu, S. Zhang, F. Liu, H. Yang, W. Huang, Microstructure and fatigue crack growth behavior of Inconel 718 superalloy manufactured by laser directed energy deposition, Int. J. Fatigue 143 (2021) 106005.
[62] Y. Gao, Y. Ding, J. Chen, J. Xu, Y. Ma, X. Wang, Effect of twin boundaries on the microstructure and mechanical properties of Inconel 625 alloy, Mater. Sci. Eng. A 767 (2019) 138361.
[63] D. Fournier, A. Pineau, Low cycle fatigue behavior of inconel 718 at 298 K and 823 K, Metall. Trans. A. 8 (1977) 1095.
[64] ISO, Metallic Materials — Unified Method of Test for the Determination of Quasistatic Fracture Toughness, 2016, pp. 1–98.
[65] U. Krupp, Crack Propagation: Microstructtural Aspects Fatigue Crack Propagation in Metals and Alloys, John Wiley & Sons, 2007, pp. 135–206.
[66] H.Y. Li, H.L. Sun, P. Bowen, J.F. Knott, Effects of compressive residual stress on short fatigue crack growth in a nickel-based superalloy, Int. J. Fatigue 108 (2018) 53–61.
[67] Y. Yamada, J.C. Newman, Crack closure under high load-ratio conditions for Inconel-718 near threshold behavior, Eng. Fract. Mech. 76 (2) (2009) 209–220.
[68] X. Hu, Z. Xue, T. Ren, Y. Jiang, C. Dong, F. Liu, On the fatigue crack growth behaviour of selective laser melting fabricated Inconel 625: effects of build orientation and stress ratio, Fatigue Fract. Eng. Mater. Struct. 43 (4) (2020) 771–787.
[69] J.C. Newman, Y. Yamada, Compression precracking methods to generate near-threshold fatigue-crack-growth-rate data, Int. J. Fatigue 32 (6) (2010) 879–885.
[70] P.L. Blackwell, The mechanical and microstructural characteristics of laser-deposited IN718, J. Mater. Process. Technol. 170 (1–2) (2005) 240–246.
[71] X.-A. Hu, G.-L. Zhao, Y. Jiang, X.-F. Ma, F.-C. Liu, J. Huang, C.-L. Dong, Experimental investigation on the LCF behavior affected by manufacturing defects and creep damage of one selective laser melting nickel-based superalloy at 815 °C, Acta Metal. Sinica (English Letters) 33 (4) (2020) 514–527.
[72] M. Knezevic, S. Ghorbanpour, N.C. Ferreri, I.A. Riyad, A.D. Kudzal, J.D. Paramore, S.C. Vogel, B.A. McWilliams, Thermo-hydrogen refinement of microstructure to improve mechanical properties of Ti–6Al–4V fabricated via laser powder bed fusion, Mater. Sci. Eng. A 809 (2021) 140980.
[73] S.R. Daniewicz, N. Shamsaei, An introduction to the fatigue and fracture behavior of additive manufactured parts, Int. J. Fatigue 94 (2017) 167.
[74] P. Peralta, R. Dickerson, N. Dellan, K. Komandur, M.A. Jameel, Effects of local grain orientation on fatigue crack growth in multicrystalline fcc metallic materials, J. Eng. Mater. Technol. 127 (1) (2005) 23–32.
[75] A.R. Balachandramurthi, J. Moverare, T. Hansson, R. Pederson, Anisotropic fatigue properties of alloy 718 manufactured by Electron beam powder bed fusion, Int. J. Fatigue 141 (2020) 105898.